Published in final edited form as:
J Comput Neurosci. 2011 October ; 31(2): 305–328. doi:10.1007/s10827-010-0311-y.

Interactions of persistent sodium and calcium-activated nonspecific cationic currents yield dynamically distinct bursting regimes in a model of respiratory neurons

Justin R. Dunmyre,
Department of Mathematics and Complex Biological Systems Group, University of Pittsburgh, 301 Thackeray Hall, Pittsburgh, PA 15260, USA

Christopher A. Del Negro, and
Department of Applied Science, College of William & Mary, Williamsburg, VA 23187-8795, USA

Jonathan E. Rubin
Department of Mathematics and Complex Biological Systems Group, University of Pittsburgh, 301 Thackeray Hall, Pittsburgh, PA 15260, USA

Justin R. Dunmyre: mathemagician@gmail.com; Jonathan E. Rubin: jonrubin@pitt.edu

Abstract

The preBötzinger complex (preBötC) is a heterogeneous neuronal network within the mammalian brainstem that has been experimentally found to generate robust, synchronous bursts that drive the inspiratory phase of the respiratory rhythm. The persistent sodium (NaP) current is observed in every preBötC neuron, and significant modeling effort has characterized its contribution to square-wave bursting in the preBötC. Recent experimental work demonstrated that neurons within the preBötC are endowed with a calcium-activated nonspecific cationic (CAN) current that is activated by a signaling cascade initiated by glutamate. In a preBötC model, the CAN current was shown to promote robust bursts that experience depolarization block (DB bursts). We consider a self-coupled model neuron, which we represent as a single compartment based on our experimental finding of electrotonic compactness, under variation of g_{NaP}, the conductance of the NaP current, and g_{CAN}, the conductance of the CAN current. Varying these two conductances yields a spectrum of activity patterns, including quiescence, tonic activity, square-wave bursting, DB bursting, and a novel mixture of square-wave and DB bursts, which match well with activity that we observe in experimental preparations. We elucidate the mechanisms underlying these dynamics, as well as the transitions between these regimes and the occurrence of bistability, by applying the mathematical tools of bifurcation analysis and slow-fast decomposition. Based on the prevalence of NaP and CAN currents, we expect that the generalizable framework for modeling their interactions that we present may be relevant to the rhythmicity of other brain areas beyond the preBötC as well.

Keywords

Respiration; preBötzinger complex; Central pattern generator; Bifurcation analysis; Bursting; Slow-fast decomposition

Correspondence to: Justin R. Dunmyre, mathemagician@gmail.com.

Electronic supplementary material The online version of this article (http://dx.doi.org/10.1007/s10827-010-0311-y) contains supplementary material, which is available to authorized users.

1 Introduction

The preBötzinger complex (preBötC) of the mammalian ventral respiratory brainstem contains a heterogeneous neuronal network that generates the inspiratory phase of the respiratory rhythm (Smith et al. 1991; Feldman and Del Negro 2006). In isolation from the rest of the brainstem, the preBötC sustains robust, network-wide, rhythmic bursts that can be studied in reduced preparations *in vitro* (Smith et al. 1991). Excitatory synaptic connections between neurons within the preBötC are essential for rhythm generation, while the preBötC rhythm persists under blockade of chloride-mediated inhibition (Feldman and Smith 1989; Brockhaus and Ballanyi 1998; Shao and Feldman 1997; Ren and Greer 2006). Neurons within the preBötC are endowed with a persistent sodium (NaP) current (Paton et al. 2006) and a calcium activated nonspecific cationic (CAN) current (Pace et al. 2007a). Both currents are relevant to rhythmicity within the preBötC. The CAN current can be activated via second-messenger mediated synaptic pathways (Pace et al. 2007a). The NaP current is voltage dependent but has sub-threshold activation (Del Negro et al. 2002a; Ptak et al. 2005; Koizumi and Smith 2008), which allows it to drive square-wave bursting in a computational model and would also give it the potential to complement the CAN current by amplifying synaptic excitation. Previous analysis of preBötC activity has primarily focused on each of these currents individually, in the context of distinct neuronal models (Butera et al. 1999a; Rubin et al. 2009b). To understand how these two currents interact to promote rhythmicity of the preBötC, we present and analyze a model that includes both the CAN and NaP currents.

The NaP current has been shown to play a role in generating robust bursts in the preBötC (Paton et al. 2006; Ptak et al. 2005; Koizumi and Smith 2008; Del Negro et al. 2002a; Rybak et al. 2007), at least in certain conditions, such as when the respiratory brainstem is challenged by hypoxia, anoxia, or hypercapnia (Rubin et al. 2009a; Smith et al. 2007; Rybak et al. 2003). Butera and colleagues developed a single neuron model (henceforth called the Butera model) that included the NaP current (Butera et al. 1999a, b). This model can exhibit network bursting and reproduce important features of the *in vitro* respiratory rhythm. Recent experimental results suggest that under pharmacological nullification of the NaP current (Del Negro et al. 2001), the preBötC still generates an inspiratory-like rhythm (Pace et al. 2007b). Nevertheless, the NaP current is ubiquitous within the preBötC and given its capacity to enhance neuronal activity (Lee and Heckman 2001), investigation of the NaP current is critical to efforts to fully understand preBötC rhythmicity.

The CAN current is found in up to 96% of preBötC neurons (Pace et al. 2007a). Experimental results indicate that the CAN current plays an important role in rhythmogenesis within the preBötC (Crowder et al. 2007; Mironov 2008; Pace et al. 2007a, b). A recent model (we will call it the Rubin–Hayes model) was used to study the CAN-based mechanism for rhythmogenesis by focusing on the role of excitatory synaptic interactions in activating the CAN current (Rubin et al. 2009b). In its core form, this model included the CAN current and a Na/K ATPase electrogenic pump current. It was shown that qualitative features of model dynamics were preserved when the pump was replaced by any of a variety of other currents, including the NaP current. Analysis was done mostly in the absence of the NaP current, however, to focus on emergent network properties achieved through recruitment of postsynaptic burst-generating conductances by network activity.

In this work, we analyze a unified model by extending the core Rubin–Hayes model to include the NaP current, with all of its associated dynamic effects. This is a crucial step in understanding the rhythmicity of the preBötC. Indeed, although the previous modeling work done on these neurons for the most part separated out the CAN and NaP components of preBötC dynamics, it is likely that in the majority of preBötC neurons, it is the interaction of

these currents that produces the cellular activity that underlies the bursting rhythm. Our unified model provides a framework with which we can understand this interaction.

We use a slow-fast decomposition involving three slow variables to analyze dynamics of the unified model. We approach this problem by reviewing bifurcation mechanisms present in the NaP-only and CAN-only limits of the unified model, which have one and two slow variables, respectively, and then consider how these interact when both currents are present. Specifically, in Section 2, we introduce the unified model. In Section 3, we review, in the context of the unified model, the mechanisms by which the Butera model and Rubin–Hayes model generate bursting rhythms. Section 4 discusses the particulars of our numerical implementations of the unified model. In Section 5 and Section 6 we provide an analysis of the unified model by considering dynamic regimes that emerge under variation of the CAN and NaP conductances. Section 7 highlights the coexistence of bursting and tonically active solutions for some regions of conductance space. Overall, our work shows that the interaction of the synaptically activated CAN conductance with the voltage dependent NaP conductance yields a rich spectrum of behaviors, most of which are prevalent in experimental recordings of neurons of the preBötC. These results suggest that the diversity of observed preBötC neuron outputs reflects an intrinsic heterogeneity across neurons in this population, which should be taken into account in future preBötC network models.

2 Preliminaries

We present and analyze a model that extends the Rubin–Hayes model to include the NaP current. As a starting point for developing this model, we used the Rubin–Hayes model containing the CAN current together with a Na/K ATPase pump. In the Rubin–Hayes model, individual model neurons isolated from synaptic inputs can be quiescent or tonically active, with transitions between these regimes governed by the reversal potential, E_L, of the leak current, or equivalently by I_{app}, the applied current. Excitatory synaptic coupling between two tonically active model neurons, or between a quiescent model neuron and a tonically active model neuron, allows the pair to burst via interactions of the CAN current and the Na/K ATPase pump. We analyze a self-coupled model neuron that, considered in synaptic isolation, would be tonically active. We review the mechanisms underlying the bursting behavior in the Rubin–Hayes model resulting from synaptic excitation in Section 3.2. We model the NaP current based on the data given for the Butera model (Butera et al. 1999a).

The Butera model differs from the Rubin–Hayes model in that isolated model neurons, without self-coupling, may have quiescent, bursting, or tonically active spiking patterns, with transitions between these dynamics as appropriate parameters are varied (Purvis et al. 2007). In the Butera model, introducing self-coupling for a model neuron that would intrinsically be tonically active may yield a bursting rhythm (Best et al. 2005). Quiescent and tonically active model neurons may also be coupled together to generate a bursting rhythm (Rubin 2006; Dunmyre and Rubin 2010). In the Butera model, the NaP current is responsible for transitions from the silent to the active phase and for the return from the active phase to the silent phase, as reviewed in Section 3.1.

Parameters have been adjusted from those values found in Rubin et al. (2009b) and Butera et al. (1999a) such that the unified model can be tuned to generate qualitatively identical dynamics to the Rubin–Hayes model and the Butera model. Using the notation $\dot{x}$ for the time derivative of the variable x, the unified model is

$$\dot{v}=-\{I_L(v)+I_{Na}(v,h,m)+I_{\text{K}}(v,n)+I_{\text{NaP}}(v,hp)+I_{\text{CAN}}(v,Ca)+I_{\text{pump}}(Na)-I_{\text{app}}+I_{\text{syn}}(v,s)\}/C_m \quad (1)$$

$$\dot{h}=(h_\infty(v)-h)/\tau_h(v) \tag{2}$$

$$\dot{m}=(m_\infty(v)-m)/\tau_m(v) \tag{3}$$

$$\dot{n}=(n_\infty(v)-n)/\tau_n(v) \tag{4}$$

$$\dot{Ca}=\varepsilon_{Ca}(k_{IP_3}s-k_{Ca}(Ca-Ca_{\text{base}})) \tag{5}$$

$$\dot{Na}=\alpha(-I_{\text{CAN}}(v,Ca)-I_{\text{pupm}}(Na)) \tag{6}$$

$$\dot{hp}=\varepsilon_{hp}(hp_\infty(v)-hp)/\tau_{hp}(v) \tag{7}$$

$$\dot{s}=((1-s)s_\infty(v)-k_s s)/\tau_s \tag{8}$$

where ε_{Ca}, α, and ε_{hp} are relatively quite small, and $I_L(v)=g_L(v-E_L)$, $I_{Na}(v,h,m)=g_{Na}m^3h(v-E_{Na})$, $I_{\text{K}}(v,n)=g_{\text{K}}n^4(v-E_{\text{K}})$, $I_{\text{syn}}(v,s)=g_{\text{syn}}s(v-E_{\text{syn}})$, $I_{\text{CAN}}(v,Ca)=g_{\text{CAN}}(v-E_{\text{CAN}})/(1+\exp((Ca-k_{\text{CAN}})/\sigma_{\text{CAN}}))$, $I_{\text{NaP}}(v,hp)=g_{\text{NaP}}mp_\infty(v)hp(v-E_{Na})$, $I_{\text{pump}}(Na)=\phi(Na)-\phi(Na_{\text{base}})$, where $\phi(x)=x^3/(x^3+k_{Na}^3)$. For each $x\in\{h,hp,mp,n,s\}$, the function $x_\infty(v)$ takes the form $x_\infty(v)=\{1+\exp[(v-\theta_x)/\sigma_x]\}^{-1}$. Also for each $x\in\{h,hp,m,n\}$, the function $\tau_x(v)$ is given by $\tau_x(v)=\bar{\tau}_x/\cosh[(v-\theta_x)/(2\sigma_x)]$. In Table 1 we record the baseline parameter values used for Eqs. (1)–(8). A value for E_L is included, although we also comment on variations away from this baseline. Values of g_{CAN} and g_{NaP} are discussed throughout the text, so these parameters do not appear in Table 1.

In the Rubin–Hayes model and the unified model (1)–(8), the value for k_{IP_3} is large and represents the effects of a signaling cascade that begins with presynaptic glutamate release and terminates with the release of intracellular calcium stored in the postsynaptic endoplasmic reticulum. When enough intracellular calcium is released (represented by $Ca\approx k_{\text{CAN}}$) the CAN current activates. The Rubin–Hayes model includes an outward current denoted $I_{\text{pump}}(Na)$ with corresponding dynamic variable Na, which represents the effects of ATPase pumps that are activated during CAN current dominated activity (Rubin et al. 2009b).

When two neurons modeled by Eqs. (1)–(8) are coupled with excitatory synapses, the pair can produce robust bursts analogous to those exhibited by the Rubin–Hayes model, when $g_{\text{NaP}}=0$, or to those exhibited by the Butera model, when $g_{\text{CAN}}=0$. With the unified model, we seek to analyze the forms of rhythmic activity produced by interactions of the CAN and NaP currents. To understand this interaction, we systematically vary g_{CAN}, the conductance of the CAN current, and g_{NaP}, the conductance of the NaP current.

In a real preBötC neuron, synaptic recruitment of the CAN current and the Na/K ATPase pump activity occurs primarily in dendrites (Pace and Del Negro 2008; Mironov 2008;Morgado-Valle et al. 2008), whereas sodium channels are likely to be most prevalent near the axon hillock, where they can strongly influence action potential generation. However, simultaneous somatic voltage recordings and dendritic calcium imaging from preBötC neurons suggest that preBötC neurons are electrotonically compact. Figure 1 shows an example of the temporal proximity of somatic and dendrite responses, which is

representative of a large set of recordings (Del Negro et al. 2010). In particular Fig. 1(e) demonstrates that the difference between the time when the onset of activity occurs in the dendrite (green trace in panel (e)) and the time when activity begins in the soma (black trace at the top of panel (e)) is sufficiently small that we may justify using a one compartment model, which simplifies the analysis. Another way we have simplified analysis is by focusing on one self-coupled model neuron, instead of a network of two model neurons. We provide numerical justification for this simplification in Section 4.

Our primary tool for analysis will be geometric singular perturbation theory (Fenichel 1979) (for thorough review see Jones 1994). This analysis exploits the fact that ε_{Ca}, α and ε_{hp} are small, and so *Ca, Na, hp* (the "slow subsystem") evolve on a timescale separate from the dynamic variables *v, h, m, n, s* (the "fast subsystem"). Here we briefly summarize the interactions of the slow and fast subsystems. From the perspective of the fast subsystem, the slow subsystem's dynamic variables are fixed at some values. The fast subsystem then approaches some stable orbit or critical point based on the current values of the slow variables. From the slow subsystem's perspective, the dynamics of the fast subsystem is instantaneous. Based on the asymptotic limit of the fast subsystem dynamics, the slow subsystem slowly evolves. This drift updates the appropriate stable orbit for the fast subsystem, but the fast subsystem instantly tracks these updates, and the slow subsystem continues to drift in a way that is determined by the fast subsystem's limits.

3 Review of the limiting cases $g_{CAN=0}$ and $g_{NaP=0}$

We begin our analysis by reviewing model dynamics in the two extremal parameter regimes, $g_{CAN} = 0$ and $g_{NaP} = 0$. Analysis of these regimes isolates key mechanisms that will combine to yield the rich dynamics of the general case.

3.1 Dynamics without the CAN current

First, we set $g_{CAN} = 0$ and allow g_{NaP} to vary for a self-coupled model neuron. With $g_{CAN} = 0$, we can safely ignore the calcium dynamics given in Eq. (5) and the sodium dynamics will equilibrate at $Na = Na_{base}$. Thus, after a transient, we need only consider one slow variable, *hp*, which simplifies the analysis. In this case, the model is similar to the Butera model, though the parameter values differ slightly. Importantly, the bifurcation structure is similar to the one from the Butera model (see Best et al. 2005). Here we will briefly recall how a slow-fast decomposition can be used to describe the dynamics in the case $g_{CAN} = 0$. First we present the bifurcation structures associated with Eqs. (1)–(4) and (8) in Fig. 2 by projecting the bifurcation diagram generated by treating *hp* as a parameter, along with the graph of the curve satisfying equation $hp' = 0$ (also called the *hp*-nullcline), into (*v, hp*) coordinates.

We have marked three key features in Fig. 2, a saddle-node (SN) bifurcation (visible in the inset), a family P of stable periodic orbits, and the family's termination point: a critical point of the fast subsystem (1)–(4) and (8) that is the asymptotic limit of a homoclinic orbit (HC). At the SN bifurcation the family of asymptotically stable critical points of the fast subsystem that correspond to quiescence ceases to exist. The family P is born in a supercritical Andronov–Hopf (AH) bifurcation at $hp > 1.2$ but is is not visible in Fig. 2.

The features illustrated in Fig. 2 will be visited in succession by the evolving trajectory to create the dynamics for the $g_{CAN} = 0$ system. We will work in the $\varepsilon_{hp} = 0$ limit so that the methods of geometric singular perturbation theory allow us to first consider the slow variable *hp* as fixed. For each fixed $hp \in [0, 1]$ each solution of the fast subsystem is quickly attracted to one of the stable structures highlighted in Fig. 2.

To facilitate our analysis we introduce the following notation. Considering hp fixed as a parameter, we call (v, h, m, n, s) the fast subsystem, with associated fast dynamics given by Eqs. (1)–(4) and (8).

Let $x \cdot t$ be the result of applying the flow of the fast dynamics to initial condition x for time t. Allow $d(x, y)$ to be the usual euclidean distance between points $x = (v_x, h_x, m_x, n_x, s_x)$ and $y = (v_y, h_y, m_y, n_y, s_y)$, that is, $d(x,y)=\sqrt{(v_x - v_y)^2+(h_x - h_y)^2+\ldots+(s_x - s_y)^2}$. We use the dynamics of Eqs. (1)–(4) and (8) to define $F_{g_{\mathrm{CAN}}=0}(hp, x_0) = \{x$: for fixed hp and any given $\delta > 0$ there exists $t_n \to \infty$ such that for each t_n, $d(x_0 \cdot t_n, x) < \delta\}$. Note that $F_{g_{\mathrm{CAN}}=0}(hp, x_0)$ can be thought of as $\lim_{t\to\infty} x_0 \cdot t$ for hp fixed, when this limit exists. $F_{g_{\mathrm{CAN}}=0}(hp, x_0)$ may be either a nontrivial orbit or a critical point and may depend critically on x_0 for choices of hp where the fast subsystem exhibits bistability. We construct a solution for the full system by allowing hp to drift based on the dynamics of Eq. (7) averaged over $F_{g_{\mathrm{CAN}}=0}(hp, x_0)$. We define hp_{SN} to be the hp coordinate of the SN bifurcation. In Fig. 2 the AH bifurcation (with hp-coordinate hp_{AH}) is not seen because it occurs at $hp_{AH} > 1.2$. Further, for hp fixed in $[0, hp_{SN})$, we define $Q(hp)$ to be the unique stable critical point of the fast subsystem corresponding to quiescence for that fixed hp, see Fig. 2. We will call hp_{HC} the hp coordinate of the homoclinic orbit. For $hp_{HC} \le hp < 1$ we define $P(hp)$ to be the unique stable periodic orbit with large amplitude and high voltage corresponding to fast subsystem spiking for that given value of hp, see Fig. 2.

Without loss of generality, we begin our analysis of the model dynamics with $g_{\mathrm{CAN}} = 0$ and an initial condition (hp, x_0) on the lower stable branch in Fig. 2; that is, $(hp, x_0) = (hp, Q(hp))$ for $0 < hp < hp_{SN}$. $F_{g_{\mathrm{CAN}}=0}(hp, x_0) = Q(hp)$ is below the hp-nullcline, so that hp will slowly begin to increase toward $hp_\infty(v)$. As hp slowly increases, $F_{g_{\mathrm{CAN}}=0}(hp, x_0) = Q(hp)$ initially persists. If the hp-nullcline intersects the curve of stable quiescent states, then the system converges to this intersection point, and the resultant solution will exhibit quiescent dynamics. Otherwise, $hp > hp_{SN}$ eventually holds, and $Q(hp)$ is not defined for such values of hp. For $hp_{AH} > hp > hp_{SN}$, $F_{g_{\mathrm{CAN}}=0}(hp, x_0) = P(hp)$, so a spiking or active phase begins once $hp > hp_{SN}$.

During the active phase, the relation $F_{g_{\mathrm{CAN}}=0}(hp, x_0) = P(hp)$ is maintained, based on the x_0 values visited. If the right hand side of Eq. (7) averaged over $P(hp)$ is negative for each fixed $hp \in (hp_{HC}, hp_{SN}]$, then there is a negative net drift for hp, so that hp decreases until $hp \approx hp_{HC}$. The location of the hp-nullcline relative to the homoclinic orbit will determine the resultant dynamics of the solution. More precisely, let $T(P(hp))$ be the period of $P(hp)$ and let $D(hp)=\varepsilon_{hp}\int_0^{T(P(hp))}(hp_\infty(v) - hp)/\tau_{hp}(v)$ where (v, m, n, h, s) evolve according to $P(hp)$. The net drift of hp across the homoclinic is $D=\lim_{hp\to hp_{HC}^+} D(hp)$. Suppose $D < 0$. Under this assumption, $hp < hp_{HC}$ eventually holds (and $P(hp)$ is no longer defined) and again $F_{g_{\mathrm{CAN}}=0}(hp, x_0) = Q(hp)$, resulting in the termination of the active phase, after which the full cycle repeats. Such dynamics represents square-wave bursting. On the other hand, if $D \ge 0$, even if $hp < hp_{HC}$ for some time, then eventually $hp > hp_{HC}$ again, and $F_{g_{\mathrm{CAN}}=0}(hp, x_0) = P(hp)$ for all subsequent time. The full system will eventually settle onto a periodic orbit, resulting in tonic spiking.

Modulation of g_{NaP} or E_L shifts the location of the SN bifurcation and the location of the homoclinic orbit. For some range of $E_L \le -61$ and $E_L = -61$ in particular, increasing g_{NaP} from 0 to 5, the stable dynamics changes from quiescence to bursting, and eventually from bursting to tonic spiking. For some range of $E_L \ge -60$ and $g_{\mathrm{NaP}} \in [0, 5]$, the full system always exhibits tonic spiking.

3.2 Dynamics without the NaP current

We now consider a self-coupled model neuron with $g_{NaP} = 0$ and g_{CAN} nonzero. With $g_{NaP} = 0$, we may safely ignore the dynamics of hp, and so may reduce our system to one that has two slow variables: Ca and Na. In this case, with the exception of a few parameter values, the model is the same as the Rubin–Hayes model (Rubin et al. 2009b). For a sample voltage trace of a burst when $g_{NaP} = 0$, together with its projection into the (Na,Ca) plane, see Fig. 3. There are several bifurcation structures we must consider to explain the dynamics when $g_{NaP} = 0$. In Fig. 4, we present the bifurcation diagram of the fast subsystem projected into (Ca, v) coordinates with $Na > Na_{base}$ fixed. As in the $g_{CAN} = 0$ regime, there is a supercritical AH bifurcation that gives rise to a family of small amplitude periodic orbits, which quickly coalesce with a family of unstable periodic orbits at a SNP bifurcation; it is important to note that the Ca-coordinate of the AH bifurcation will be attainable by the full system, unlike the $g_{CAN} = 0$ case. The unstable family of periodic orbits meets the stable family of periodic orbits P at another SNP bifurcation. P contains periodic orbits with large amplitude and generally short period, again representative of neuronal spiking. As above, P terminates at a homoclinic orbit; however, this homoclinic orbit precisely coincides with a SN bifurcation, resulting in a saddle-node on an invariant circle (SNIC) bifurcation. In this section, we consider two slow variables, but our definitions will be analogous to those in Section 3.1. In Section 3.1 we defined $Q(hp)$ as the branch of stable quiescent critical points for the fast subsystem. Those critical points were not defined for $hp > hp_{SN}$. Analogously, in this section, instead of a single SN bifurcation point, there is a curve of SNIC bifurcations in the (Ca, Na) plane. Setting $Ca = Ca_{base}$ and considering Na as a bifurcation parameter, there is a SNIC bifurcation of the critical points corresponding to quiescence at $Na = Na_{SNIC}$. For $Na > Na_{SNIC}$ we define $Ca_{SNIC}(Na)$ to be the unique Ca coordinate of the curve of SNIC bifurcations. For (Ca, Na) such that $Na > Na_{SNIC}$ and $Ca < Ca_{SNIC}(Na)$ there is a unique stable critical point of the fast subsystem, $Q(Ca, Na)$, corresponding to hyperpolarized quiescence. In particular, $Ca_{base} < Ca_{SNIC}(Na)$ for almost all $Na > Na_{SNIC}$.

Similarly to Section 3.1, we use the dynamics of Eqs. (1)–(4), (8) to define $F_{g_{NaP}=0}(Ca, Na, x_0) = \{x$: for fixed (Ca, Na) and any given $\delta > 0$ there exists $t_n \to \infty$ such that for each t_n, $d(x_0 \cdot t_n, x) < \delta\}$. Again, $F_{g_{NaP}=0}(Ca, Na, x_0)$ may be either a nontrivial orbit or a critical point. We use this definition to consider various types of trajectories for the full system. We begin our construction with $Ca = Ca_{base}$ and $Na > Na_{SNIC}$ so that $F_{g_{NaP}=0}(Ca, Na, x_0) = Q(Ca, Na)$. In this state, $s \approx 0$ and thus $\dot{Ca} \approx 0$, and we need only consider the Na dynamics, which will initially cause Na to decrease toward Na_{base}. If $Na_{SNIC} < Na_{base}$, then Na will stagnate at Na_{base}, resulting in a solution to the full system that exhibits quiescence. On the other hand, if $Na_{SNIC} > Na_{base}$, the system may exhibit bursting or tonic spiking dynamics. As Na decreases toward Na_{base}, eventually $Na < Na_{SNIC}$ holds and $Q(Ca, Na)$ is no longer defined; the full system exits the quiescent state, see Fig. 5.

For fixed Na, treating Ca as a bifurcation parameter yields two SNP bifurcations, which we label as ISNP ("inner SNP"), for the one with a lower Ca coordinate, and OSNP ("outer SNP"), for the bifurcation at higher Ca coordinate. We define $Ca_{ISNP}(Na)$ to be the Ca coordinate of ISNP for the given value of Na, and similarly, $Ca_{OSNP}(Na)$ is defined to be the Ca coordinate of OSNP for the given value of Na. For $Ca_{SNIC}(Na) \leq Ca < Ca_{OSNP}(Na)$ we can define $P(Ca, Na)$ to be the unique high voltage large amplitude stable periodic orbit of the fast subsystem that corresponds to spiking.

As the full system exits the quiescent state, it follows that $F_{g_{NaP}=0}(Ca, Na, x_0) = P(Ca, Na)$. The model neuron is self-coupled, and as a result of the spiking the s dynamic variable increases, which induces a positive drift in Ca, see Eq. (5). Increased Ca activates the CAN current, which for sufficiently high g_{CAN} leads to increased spiking frequency. This increased spiking frequency further drives Ca by sustaining a higher synaptic level s, see

Eqs. (1) and (8). The dynamics may enter a voltage-dependent spike inactivation state called depolarization block, and to explain this, we consider the location of the AH bifurcation relative to the trajectory of the slow subsystem. There is a curve of AH bifurcations in the (Ca, Na) plane, so we define $Ca_{AH}(Na)$ to be the Ca coordinate of the AH bifurcation for a provided value of Na. For (Ca, Na) satisfying $Ca_{AH}(Na) < Ca$, we define $DB(Ca, Na)$ to be the unique stable critical point of the fast subsystem corresponding to depolarization block (e.g., the solid branch of critical points near $v = -20$ in Fig. 4). As Ca increases, eventually $Ca > Ca_{\mathrm{OSNP}}(Na) > Ca_{AH}(Na)$ holds, and $P(Ca, Na)$ is no longer defined; $F_{g_{\mathrm{NaP}}=0}(Ca, Na, x_0) = DB(Ca, Na)$ so that the dynamics no longer exhibits spiking. Instead, through damped oscillations, it winds down to the depolarization block state.

With the full system in depolarization block, the s dynamic variable decays due to the spike attenuation (see Eq. (8), and in particular $s_\infty(v)$ and θ_s in Section 2). From Eq. (5) we note that low levels of s cause Ca to decay, so that $Ca < Ca_{AH}(Na)$ eventually holds. For (Ca, Na) satisfying $Ca_{\mathrm{ISNP}}(Na) < Ca < Ca_{AH}(Na)$, we define $L(Ca, Na)$ to be the unique high voltage low amplitude stable periodic orbit of the fast subsystem corresponding to the given (Ca, Na) pair. For $Ca_{\mathrm{ISNP}}(Na) < Ca < Ca_{AH}(Na)$ there is bistability between $L(Ca, Na)$ and $P(Ca, Na)$ for the fast subsystem; however, a solution just exiting depolarization block will be in the basin of attraction for $L(Ca, Na)$. Periodic orbits for $L(Ca, Na)$ have a maximal voltage less than θ_s; see Fig. 4 for an example of this situation. These sub-threshold oscillations do not yield an increase in the s dynamic variable, so that Ca continues to have a negative drift, at least until $Ca < Ca_{\mathrm{ISNP}}(Na)$, so that $L(Ca, Na)$ is no longer defined and $F_{g_{\mathrm{NaP}}=0}(Ca, Na, x_0) = P(Ca, Na)$. However, due to the activated CAN current, Na continues to have a positive net drift throughout the active phase that we have described, see Eq. (6). As Na increases, so does $Ca_{\mathrm{SNIC}}(Na)$. If the combined changes in Na and Ca push $Ca < Ca_{\mathrm{SNIC}}$, then $P(Ca, Na)$ is not defined, yielding $F_{g_{\mathrm{NaP}}=0}(Ca, Na, x_0) = Q(Ca, Na)$ so that the full system returns to the silent phase. We summarize the (Na, Ca) coordinates corresponding to different dynamics for $F_{g_{\mathrm{NaP}}=0}(Ca, Na, x_0)$ in Fig. 5.

A solution that encompasses all of these components has a burst that exhibits depolarization block during its active phase, which we will call a DB burst. If g_{CAN} is low, then, for $Na \geq Na_{\mathrm{base}}$, $Ca_{AH}(Na)$ may be beyond the maximum attainable value of Ca, so the model neuron will not reach the depolarization block state, see Section 5.5. This may lead either to square-wave bursting or to tonic activity. We say that a function $f(x)$ blows up for finite $x = x_0$ if $\lim_{x \to x_0} f(x) = \infty$. When the coordinate of a bifurcation blows up, the trajectory may be captured by this bifurcation. For instance, if $Ca_{\mathrm{SNIC}}(Na)$ blows up for finite $Na = Na_0$ then as Na approaches Na_0, the trajectory's Ca and Na coordinates satisfy $Ca < Ca_{\mathrm{SNIC}}(Na)$, and so $F_{g_{\mathrm{NaP}}=0}(Ca, Na, x_0) = Q(Ca, Na)$ and we say that the trajectory has been captured by the SNIC bifurcation. Specifically, if g_{CAN} is low, then $Ca_{\mathrm{SNIC}}(Na)$ may blow up for finite Na, see Section 5.6.

If the activated CAN current can pull Na up to such a value that the $Ca_{\mathrm{SNIC}}(Na)$ blows up, then $F_{g_{\mathrm{NaP}}=0}(Ca, Na, x_0) = Q(Ca, Na)$. Thus, the trajectory will have a period of quiescence, so that Ca and Na will decay. As Na decays during the quiescence, $Ca_{\mathrm{SNIC}}(Na)$ takes finite values again. Eventually $Na < Na_{\mathrm{SNIC}}$ holds and triggers re-entry to the active phase, which, via activation of the CAN current, brings Na high enough that $Ca_{\mathrm{SNIC}}(Na)$ blows up, resulting in a return to the silent phase. A solution with such dynamics exhibits square-wave bursting with a long period and we note that this version of square-wave bursting is distinct from the square-wave bursts see in Section 3.1. Should this blowup of the $Ca_{\mathrm{SNIC}}(Na)$ not occur, the resultant solution has no way to return to the silent phase and so will be tonically active.

The dynamics of the $g_{NaP} = 0$ system depends on E_L as well. If $E_L \leq -61$, then $Na_{base} > Na_{SNIC}$, so that the solution cannot enter the active phase and quiescence results. If $E_L = -60$, then increasing g_{CAN} from 0 to 5 first yields tonically active solutions and then DB bursting solutions. For $E_L = -59.5$, increasing g_{CAN} from 0 to 5 first yields solutions that are tonically active, then square-wave bursting, then tonic activity again, and finally DB bursting. Desirable bursting solutions persist for a range of $E_L \geq -59.5$; however, when E_L is not sufficiently negative, I_{pump} is unable to terminate the burst by causing a prolonged silent phase (Rubin et al. 2009b). Instead, for sufficiently high g_{CAN} and E_L, the trajectory will wind back and forth through the AH bifurcation, resembling an elliptic burster. The mechanisms underlying these different solutions will be described in detail, for the more general case with both I_{NaP} and I_{CAN} in the model, in Sections 5 and 6.

4 Numerics

Most of our numerical work was done in the MAT-LAB programming language (The MathWorks, Natick, MA). Systems such as our unified model that have multiple timescales are stiff, so to speed up integration we used a C implementation of the CVODE package from SUNDIALS (Hindmarsh et al. 2005), interfaced with MATLAB via the mex command. Two dimensional bifurcation diagrams such as Fig. 2 were generated with XPPAUT (Ermentrout 2002), and three dimensional bifurcations were created by the MATCONT package for MATLAB (Dhooge et al. 2003) as well as XPPAUT. XPPAUT files for the unified model are available as electronic supplementary material.

In Fig. 6, we present a colorization of (g_{NaP}, g_{CAN}) parameter space based on the dynamics of the model under different parameter choices, using blue for quiescence, black for tonic, and green for bursting. To classify a parameter set based on neuronal activity, we use initial conditions corresponding to the silent phase, with elevated Na and low Ca and hp, and after a transient of 10,000 msec, we apply an algorithm to the spiking pattern of the model neuron recorded over the next 9,999 msec. The algorithm records that the model neuron has spiked each time $V = 0$ and $V' > 0$, since most spikes peak at about $V = 20$, and V stays below 0 during both the spike attenuation leading into depolarization block that sometimes occurs and the sub-threshold oscillations that emerge upon exit from depolarization block. If there are no spikes after the initial transient, then we classify the model neuron as quiescent. Otherwise, we compute the standard deviation of the interspike intervals (ISI). The ISI of a tonically active model neuron will have a standard deviation very close to zero milliseconds. On the other hand, due to the long time between the last spike of a burst and the first spike of the next burst, in the bursting case the standard deviation of the ISI is significantly increased relative to the tonically active case. We classified the model neurons as follows: if the standard deviation of the ISI was less than 10 msec, we considered the model neurons to be tonically active; otherwise, they were considered to be bursting. All of the tonically active model neurons observed before automating the procedure had ISI standard deviations well below 10 msec. Most bursting solutions yielded ISIs with standard deviations greater than 50 msec, so a threshold of 10 msec is reasonable for partitioning the parameter space.

We include white labels in Fig. 6 to facilitate later discussion. Figure 7 provides representative voltage traces from these labeled regions. The bursting dynamics in region II (Fig. 7(a)) is square-wave bursting as seen in the Butera model (Butera et al. 1999a), while that in region III (Fig. 7(b)) is DB bursting as seen in the Rubin–Hayes model (Rubin et al. 2009b). Both of these are prevalent in voltage traces recorded from mouse preBötC slices, as are the patterns found in region * (Fig. 7(c)). Figure 8 gives several sample recordings and agrees well with model output for the various bursting regimes.

In Fig. 9 we present a colorization of (g_{NaP}, g_{CAN}) parameter space for two reciprocally coupled model neurons that have slightly different initial conditions but the same values for all other parameters. For automated dynamics detection, the above algorithm had to be modified slightly to account for the phase difference in bursts. For each model neuron, we determine the burst duration of the last recorded burst by taking the difference in times for the first spike and last spike of the burst. We define the total time of activity as the difference between the first spike of the first model neuron to enter the active phase and the last spike of the last model neuron to enter the silent phase. We define the time of shared activity as the difference between the first spike of the second model neuron to enter the active phase and the last spike of the first model neuron to enter the silent phase. If the ratio of the shared activity to the total activity was greater than 0.4, we say that the bursts were in-phase, otherwise, we say the bursts are out-of-phase. For the most part Fig. 9 looks like Fig. 6. The key difference is that, for $g_{CAN} > 3$, tonic solutions are more prevalent in the two-neuron case. Most of these tonic solutions lack spike synchrony. The precise effects of spike asynchrony are out of the scope of this work, but the primary result is that this feature allows for bistability between asynchronous tonically active solutions and bursting similar to that arising in regions II, III and * in Fig. 6. This accounts for the primary difference between Figs. 6 and 9. Except for the precise spike synchrony, all of the dynamics observed in the self-coupled case have been observed in the two-neuron case. Thus, to gain insight into the two-neuron network, a good step is to understand the self-coupled case.

Variations in E_L have been used to explore robustness of model dynamics in past work, for various reasons (see Discussion). We generated Fig. 6 with $E_L = -61$, although the figure would be qualitatively similar for a range of E_L values. In particular, for $E_L < -61$, a higher value of g_{NaP} is required for solutions to be able to enter the active phase, so all of the regions will shift to the right in g_{NaP} space. On the other hand, for $E_L > -61$ and large enough such that the system fails to produce quiescence or bursts when $g_{CAN} = 0$, then the $g_{CAN} \neq 0$ case will not exhibit region I-like or region II-like dynamics, but the other regions persist. We note that region * is lost for a value of E_L close to that which causes the loss of region II. For E_L insufficiently negative, I_{pump} and the NaP current will be unable to cause a prolonged silent phase (as seen in the $g_{NaP} = 0$ case), and the system may exhibit activity that resembles elliptic bursts.

5 Analysis of unified model dynamics

In this section, we analyze the mechanisms by which the solutions observed in each marked region of Fig. 6 come about. Figure 6 was generated with $E_L = -61$ and with initial conditions corresponding to the quiescent state, as described in Section 4. We elected $E_L = -61$ for this analysis because when $g_{CAN} = 0$, we have quiescent, bursting, and tonic spiking solutions, depending on the values of other parameters, in the presence of self-coupling.

For $g_{NaP} \neq 0$, for fixed $hp > 0$ and for fixed $Na > Na_{base}$, the bifurcation diagram for the fast subsystem generated by treating Ca as a bifurcation parameter is similar to Fig. 4. When $g_{NaP} \neq 0$, but $hp = 0$, the bifurcation diagram is the same as Fig. 4, because hp and g_{NaP} are multiplied together in Eq. (1) and do not appear anywhere else in the fast subsystem. However, for $hp > 0$, the SNIC bifurcation from the $hp = 0$ case decomposes into a SN bifurcation and a separate homoclinic bifurcation as in Fig. 2. The unstable critical point to which the homoclinic orbit converges as $t \to \pm\infty$ will be called a homoclinic point. For sufficiently small hp, we may approximate the Ca and Na coordinates of the homoclinic point with the coordinates of the SN bifurcation. Again, we will work in the (ε_{Ca}, α, ε_{hp}) = (0, 0, 0) limit and allow $F(Ca, Na, hp, x_0) = \{x$: for fixed (Ca, Na, hp) and any given $\delta > 0$ there exists $t_n \to \infty$ such that for each t_n, $d(x_0 \cdot t_n, x) < \delta\}$. As before, $F(Ca, Na, hp, x_0)$ may be a critical point or a nontrivial orbit. In Fig. 10, by treating Ca, Na, hp as bifurcation

parameters, we present some examples of bifurcation structures for the fast subsystem; in particular, we include a surface of SN bifurcations (SN surface), a surface of AH bifurcations (AH surface), as well as a surface of homoclinic points (HC surface). Indeed, except for the different values of E_L used when generating Figs. 5 and 10, these figures are closely related; Fig. 5 corresponds to the $hp = 0$ plane of Fig. 10. We set $Ca_{SN}(Na, hp)$, $Ca_{AH}(Na, hp)$, and $Ca_{HC}(Na, hp)$ to be the Ca coordinates of the SN surface, AH surface, and HC surface for each given (Na, hp). We will also define $Ca_{\mathrm{ISNP}}(Na, hp)$ and $Ca_{\mathrm{OSNP}}(Na, hp)$ to be the Ca coordinates of the two SNP surfaces, analogous to the corresponding curves in Fig. 5. For $X \in \{SN, AH, HC, ISNP, OSNP\}$ we say that the trajectory intersects or reaches the surface X if the trajectory's Ca, Na, hp coordinates satisfy $Ca = Ca_X(Na, hp)$. In general, a transition from the silent phase to the active phase occurs when the trajectory intersects the SN surface transversely, and hence crosses through it, through increases in hp or Ca or decreases in Na. A transition from the active phase to the silent phase occurs when the trajectory crosses the HC surface via decreases in hp or Ca. An increase in Na promotes such a transition by bringing the surface to larger hp and Ca values (Figs. 10 and 11) but will not achieve this transition on its own due to the curvature of the relevant part of the HC surface.

For the following, we assume that initially, $Na > Na_{\mathrm{base}}$ and $0 \le hp \le 1$. As in Sections 3.1 and 3.2, for (Ca, Na, hp) such that $Ca < Ca_{SN}(Na, hp)$, there is a unique stable critical point for the fast subsystem corresponding to hyperpolarized quiescence, $Q(Ca, Na, hp)$.

For (Ca, Na, hp) such that $Ca_{HC}(Na, hp) < Ca < Ca_{\mathrm{OSNP}}(Na, hp)$ there is a unique large amplitude high voltage stable periodic orbit of the fast subsystem, $P(Ca, Na, hp)$, corresponding to spiking. When (Ca, Na, hp) satisfy $Ca_{\mathrm{ISNP}}(Na, hp) < Ca < Ca_{AH}(Na, hp)$, there is a unique small amplitude high voltage stable periodic orbit of the fast subsystem, $L(Ca, Na, hp)$, corresponding to sub-threshold oscillations. Finally, for (Ca, Na, hp) such that $Ca_{AH}(Na, hp) < Ca$, there is a unique stable critical point of the fast subsystem, $DB(Ca, Na, hp)$, corresponding to depolarization block.

5.1 Region I

As described in Fig. 6, parameter values from region I yield quiescent solutions. We begin the analysis with $g_{\mathrm{CAN}} = 0$. Increasing g_{NaP} lowers hp_{SN}, possibly so that the hp-nullcline no longer intersects the family of quiescent critical points. We call g^*_{NaP} the critical g_{NaP} such that when $g_{\mathrm{CAN}} = 0$ the quiescent solution exists if and only if $g_{\mathrm{NaP}} < g^*_{\mathrm{NaP}}$. We note that g^*_{NaP} is the value for g_{NaP} such that the hp-nullcline intersects the surface of fast subsystem critical points precisely at the SN bifurcation point. When $g_{\mathrm{NaP}} < g^*_{\mathrm{NaP}}$, allow $hp_{\max}(g_{\mathrm{NaP}})$ to be the hp coordinate of the intersection of the hp-nullcline and branch of quiescent critical points.

When $E_L = -61$ in the case $g_{\mathrm{NaP}} = 0$, the solution is unable to escape quiescence because $Na_{\mathrm{base}} > Na_{\mathrm{SNIC}}$. Modulation of g_{CAN} will not change this, because $I_{\mathrm{CAN}}(v, Ca)$ does not contribute to $\dot{v}$ when Ca is small. With Ca decaying to Ca_{base} the slow subsystem evolves toward the point $(Ca_{\mathrm{base}}, Na_{\mathrm{base}}, hp_{\max})$, and $Ca_{\mathrm{base}} < Ca_{SN}(Na_{\mathrm{base}}, hp_{\max})$ so that $F(Ca, Na, hp, x_0) \rightarrow Q(Ca_{\mathrm{base}}, Na_{\mathrm{base}}, hp_{\max})$ and the solution exhibits quiescent dynamics forever, see Fig. 12. Similar coordinates for $0 < g_{\mathrm{NaP}} < g^*_{\mathrm{NaP}}$ yield the vertical right boundary of region I in Fig. 6, representing independence from g_{CAN}.

5.2 Region II

Trajectories found for parameter values in region II exhibit square-wave bursts typical of the Butera model, even in the presence of elevated g_{CAN}. Indeed, the dynamics here is not very different from the dynamics described in Section 3.1, with $g_{\mathrm{CAN}} = 0$. Here, we will show

how this dynamics is preserved when $g_{CAN} > 0$. With $E_L = -61$, since $Na_{base} > Na_{SN}$, we rely on hp increasing enough to cause the singular solution to cross the SN surface to initiate spiking, see for instance the $Ca = Ca_{base} = 0.05$ plane in Fig. 10. That is, after Na has decayed to Na_{base} and Ca has decayed to Ca_{base}, we need hp such that $Ca_{SN}(Na_{base}, hp) < Ca_{base}$ in order for the solution to exit the silent phase. As in Section 3.2, once the solution exits the silent phase, $F(Ca, Na, hp, x_0) = P(Ca, Na, hp)$, the solution begins spiking, and hp begins to decay. Across each spike, Ca rises to a higher level, and then Ca decays after the spike. However, the CAN current requires a certain level of Ca, namely $Ca \approx k_{CAN}$, to become active and qualitatively change the dynamics. Until $Ca \approx k_{CAN}$, Na remains near Na_{base} and the dynamics is qualitatively as in the $g_{CAN} = 0$ case.

To activate the CAN current, then, we need a certain number of spikes of $F(Ca, Na, hp, x_0)$ to occur within a certain window of time to increase s and overwhelm the decay of Ca to Ca_{base} (see Eq. (5)). The bursts in region II do not yield enough spikes to meet this condition, and decreasing hp causes a return to the silent phase exactly as with $g_{CAN} = 0$. In fact, the presence of the CAN current, even if not fully activated due to low Ca, actually aids in this transition to the silent phase. The small rise in Ca induced by the spiking activity causes enough I_{CAN} activation to increase Na slightly, especially for high g_{CAN}. Numerically, we observe that, for Ca fixed, both hp_{HC} and hp_{SN} are increasing functions of Na, see Fig. 11. Thus, the spiking activity that increases Na slightly causes an earlier crossing of hp_{HC} and return to the silent phase. Further, since hp_{SN} is an increasing function of Na, hp may be unable to cross hp_{SN} until Na decays. This has two key effects. First, the dependence on the slow decay of Na causes the solution of the full system to spend a longer time in the silent phase. Second, the singular solution crosses the SN surface with a higher hp value, which may cause more spikes to occur; however, in region II, these extra spikes never appreciably activate the CAN current. So, increasing g_{CAN} within region II changes the interburst interval, and the spike counts within bursts, but does not yield the DB bursts seen in region III (Fig. 7).

5.3 Region III

Region III contains DB bursts similar to those seen in the Rubin–Hayes model from interactions of I_{CAN} and I_{pump}. Again, the key difference arising for DB bursts in the unified model (1)–(8), compared to the Rubin–Hayes model, is that the SNIC bifurcation transforms into two separate entities, a SN bifurcation of critical points and a homoclinic bifurcation. Nevertheless, when a solution spends an extended time in the active phase, we may use the SN bifurcation as an approximation to the homoclinic orbit once the CAN current is activated. This approximation is reasonable because hp becomes very small during an extended active phase and g_{NaP} and hp are multiplied in $I_{NaP}(v, hp)$ in Eq. (1), so that during an extended active phase, the bifurcation structures approach those from the $g_{NaP} = 0$ case, where the saddle node and homoclinic do combine to form a SNIC bifurcation. In Fig. 10, we see that for $hp = 0$, the homoclinic surface and SN surface coincide as expected, supporting our claim that for low hp we may approximate the homoclinic surface by the SN surface. This approximation can also be justified by the interpretation of hp as an inactivation variable for I_{NaP}, so when hp is low there is little contribution from I_{NaP} due to inactivation. This approximation will come into play in understanding the transition to the silent phase in region III, as described below.

While $F(Ca, Na, hp, x_0) = Q(Ca, Na, hp)$, decreasing Na and increasing hp cause a decrease in $Ca_{SN}(Na, hp)$, until $Ca_{SN}(Na, hp) < Ca_{base}$, allowing the trajectory to exit the silent phase. As in both Sections 3.1 and 3.2, once $Ca_{SN}(Na, hp) < Ca_{base}$, the fast subsystem no longer has a branch of critical points corresponding to quiescence as an attractor, and $F(Ca, Na, hp, x_0) = P(Ca, Na, hp)$. The difference between region II and region III is that region III has

higher g_{NaP} than region II, resulting in faster spikes along solutions in $F(Ca, Na, hp, x_0)$, which occur fast enough to build up Ca and activate the CAN current.

By the time that Ca builds up, hp has decayed significantly, so that we may approximate the HC surface by the SN surface. With this approximation, the dynamics is similar to Section 3.2. Ca continues to build up, until $Ca > Ca_{OSNP}(Na, hp)$ holds. For $Ca > Ca_{OSNP}(Na, hp)$, $F(Ca, Na, hp, x_0) = DB(Na, hp)$, and the full system enters depolarization block. Spike attenuation due to depolarization block causes Ca to decrease and eventually $Ca < Ca_{AH}(Na, hp)$ holds, such that the solution exits depolarization block. As the trajectory exits depolarization block, $F(Ca, Na, hp, x_0) = L(Ca, Na, hp)$ and the solution has small amplitude high voltage periodic orbits, as in Section 3.2. The small amplitude of the periodic orbits do not produce enough voltage variation to yield an increase in Ca. Thus, at least until $Ca < Ca_{ISNP}(Na, hp)$ holds (and so $F(Ca, Na, hp, x_0) = P(Ca, Na, hp)$), Ca continues to decrease. Meanwhile Na has been increasing, so that it is possible that as Ca decreases, $Ca < Ca_{SN}(Na, hp) \approx Ca_{HC}(Na, hp)$ results and correspondingly $F(Ca, Na, hp, x_0) = Q(Ca, Na, hp)$. The full system returns to quiescence until Na decreases and hp increases enough to start another burst, as described above.

The variable hp plays two roles in generating a DB burst in region III. First, hp combines with Na to allow escape from the silent phase. Second, hp contributes to the spike speed-up that yields the Ca increases needed for a DB burst. One of the key features of the trajectory of the full system for region III is that in the active phase, although hp becomes small, the decrease in hp alone could not trigger a return to the silent phase. As g_{NaP} is decreased, this feature may be lost, and this brings us to region *.

5.4 Region *

Region * is characterized by solutions that feature both square-wave bursts and DB bursts. As described in Section 5.3, while the full system is in the silent phase, a sufficient decrease in Na together with an adequate rise in hp allows $Ca_{SN}(Na, hp) < Ca$, causing $F(Ca, Na, hp, x_0) = P(Ca, Na, hp)$, and the solution transitions to the active phase. During the active phase, Ca increases and hp decreases. These effects result in a race between Ca and hp. On one hand, if hp decreases so that $Ca_{HC}(Na, hp) > Ca$, the full system may return to quiescence without going into the full burst that incorporates greater plateau-like voltages, higher spiking rates, and ultimately depolarization block. Thus, this outcome results in a square-wave burst as in region II. On the other hand, if Ca increases enough to activate the CAN current, then decreasing hp alone will be unable to trigger a return to the silent phase; to terminate the burst, Ca must be decreased by the full system entering depolarization block as in region III. The winner of the race is influenced by the level of Na when the full system enters the active phase, as we shall now describe.

For Ca fixed, hp_{HC} increases as Na increases, see Fig. 11. When the trajectory enters the active phase with elevated Na, the decreasing variable hp may be able to drop to the elevated value of hp_{HC} and the net drift of hp at the homoclinic orbit may be negative. In this case, hp triggers a return to the silent phase before the CAN current can activate and cause a DB burst. The result is a square-wave burst. Such square-wave bursts, due to the fact that Ca does not exhibit a large increase, yield a net decrease in Na. After one or more square-wave bursts, the full system enters the active phase with Na low enough that hp cannot drop below hp_{HC} to trigger a return to the silent phase, resulting in a DB burst. After a DB burst, Na is elevated, and thus so is hp_{HC}, so the subsequent bursts may be square-wave. In this way, we may observe solutions with varying sequences of square-wave and DB bursts.

To illustrate this mechanism, we have plotted a trajectory of the full system projected into hp, Ca space, along with two slices of the homoclinic surface, one for lower Na and one for

higher Na, see Fig. 13. We begin on the orange section of the trajectory shown in Fig. 13(b). Here, the full system has crossed through the SN surface and entered the active phase with $hp = .8$ and $Na = 5.3$ ("start" in Fig. 13(a)). As the solution spikes, Ca experiences several abrupt but transient increases while hp decreases. The trajectory passes through the blue curve, which is the slice of the homoclinic surface corresponding to $Na = 5.1$, and even though several subsequent spikes occur, they are insufficient to keep the trajectory in the active phase. With the subsequent return to the silent phase, a square-wave burst results. In the silent phase, Na decreases to 5.051 and hp increases to about 0.6, and again the trajectory passes through the SN surface, causing the solution to re-enter the active phase. We illustrate the next part of the solution in Fig. 13 in black. Again, as the solution spikes, Ca experiences abrupt though transient increases. Now we compare the trajectory of the full system against the slice of the homoclinic surface corresponding to $Na = 5.051$, shown in magenta. This time, the trajectory crosses the homoclinic surface only briefly, immediately returning back to the other side of the surface due to a spike. Indeed, this last spike brings $Ca > k_{\mathrm{CAN}}$, activating the CAN current, and the DB burst progresses as usual, such that Na attains an elevated level (Fig. 13(b)) and then the trajectory enters the silent phase. In this way, with Na diminished by each square-wave burst until it becomes small enough to allow a DB burst, which pushes it back up again, the model may continually generate alternating square-wave and DB bursts, or perhaps sequences of two or more square-wave bursts before a DB burst, as in Figs. 7(c) and 8(d).

In recordings from preBötC neurons that alternate between DB and square-wave bursts we observe that the interburst interval following a DB burst is generally longer than the interburst interval after a square-wave burst. We highlight one example of this phenomenon in Fig. 14(a), and the preceding analysis for region * can shed some light on this situation. During a DB burst, the activated CAN current elevates Na, and hp typically decays to $hp \approx 0$ due to the prolonged activity. The next active phase begins when hp crosses hp_{SN}, which will take longer due to elevated Na (Fig. 11), even though Na is slowly decaying during the silent phase. If the subsequent burst is a square-wave burst, Na will have continued to decay, and it need not be the case that $hp \approx 0$ at the start of the silent phase. Thus, following a square-wave burst, hp is initially larger and hp_{SN} is smaller (due to decaying Na), so it takes less time for the system to attain $hp > hp_{SN}$ and enter the next active phase, see Fig. 14(b).

5.5 Region IV

As before, we begin our analysis with $Na > Na_{\mathrm{base}}$, $hp = 0$, $Ca = Ca_{\mathrm{base}}$ and $F(Ca, Na, hp, x_0) = Q(Ca, Na, hp)$. A decrease in Na toward Na_{base} and an increase in hp cause $Ca_{SN}(Na, hp) < Ca$, resulting in a transition to the active phase. As in region III, g_{NaP} is high enough so that a decrease in hp alone cannot trigger a return to the silent phase. For fixed Na, hp, we observe that $Ca_{AH}(Na, hp)$ is a decreasing function of g_{CAN}, see Fig. 15. Decreasing g_{CAN} may cause $Ca_{AH}(Na, hp)$ to blow up, in which case, $Ca < Ca_{AH}(Na, hp)$ always holds. During an extended active phase, hp decreases to a minimal value, and we are essentially in the situation from Section 3.2. Recall from Section 3.2 or Section 5.3 that to terminate the burst, we required the solution to enter depolarization block so that spike attenuation would lead to a decrease in Ca. If $Ca < Ca_{AH}(Na, hp)$ always holds, the only way to depolarization block and corresponding decrease in Ca will never occur, and tonic activity results, unless eventually $Ca_{HC}(Na, hp) > Ca$ holds. However, for most values of g_{CAN}, the value of $Ca_{SN}(Na, hp)$, and thus $Ca_{HC}(Na, hp)$, remains low relative to Ca levels of CAN driven tonic activity in region IV, even for extremely high Na, see Fig. 16. Thus, given that $Ca_{AH}(Na, hp)$ is beyond the maximal attainable value of Ca and $Ca_{SN}(Na, hp)$ remains low, $F(Ca, Na, hp, x_0) = P(Ca, Na, hp)$ and the model's activity is indeed tonic.

As we shall see in the next subsection, there are some g_{CAN} values for which $Ca_{SN}(Na, hp)$ does not remain bounded as a function of Na and hence for which significantly different model dynamics emerges.

5.6 Region V

In this section we explain how the square-wave bursts seen in Fig. 7(e), corresponding to region V, are realized. As usual, we begin in the silent phase, with Na decreasing toward Na_{base} and hp increasing. Eventually, $Ca > Ca_{SN}(Na, hp)$, $F(Ca, Na, hp, x_0) = P(Ca, Na, hp)$, and the solution enters the active phase. We note that region V has g_{NaP} values similar to those of region III, which implies that the trajectory cannot return to the silent phase simply by virtue of hp decreasing, see Section 5.3. Moreover, region V lies below the g_{CAN} value for which $Ca_{AH}(Na, hp)$ blows up, see Fig. 15. So the trajectory cannot pass through the AH surface, meaning that the full system cannot enter depolarization block and hence Ca cannot decrease to pass back through the HC surface. Instead, we find in region V that $Ca_{HC}(Na, hp)$ actually blows up as Na increases, see Fig. 17. When this blowup occurs, the trajectory is captured by the HC surface, that is, $Ca < Ca_{HC}(Na, hp)$ holds so that $F(Ca, Na, hp, x_0) = Q(Ca, Na, hp)$ and the full system returns to the silent phase.

5.7 Region VI

Regions IV and VI both feature tonically active solutions. The difference between the two regions is that in region VI, the CAN current does not become active, such that essentially the same tonic spiking dynamics as in Section 3.1, with $g_{\mathrm{CAN}} = 0$, emerges. When g_{NaP} is low, there are tonic solutions such that the spikes are not fast enough to maintain sustained levels of s sufficient to increase Ca enough to activate the CAN current. When g_{CAN} is low, even if the spike acceleration increases Ca enough to activate the CAN current, the CAN current is too weak to bring Na to values such that $Ca_{SN}(Na, 0)$ blows up (Section 5.6). Also, low values of g_{CAN} prohibit the CAN current from strongly influencing the dynamics. On the other hand, in region IV, the CAN current is strong and active during tonic spiking (Section 5.5), which yields solutions with shorter ISI. We summarize these differences graphically in Fig. 18.

6 Transitions between regions

In Section 5, we explained how particular bifurcation structures give rise to different forms of model dynamics, as indicated in Figs. 6 and 7. In this section, we estimate where the borders between dynamic regimes lie in the $(g_{\mathrm{NaP}}, g_{\mathrm{CAN}})$ plane (Fig. 6) based on criteria derived from insights presented in Section 5 and additional numerical calculations. In some cases, we numerically compute estimated boundary curves, the accuracy of which confirms the validity of our analysis. The transition criteria that we provide also allow us to predict the location of regions of bistability in the $(g_{\mathrm{NaP}}, g_{\mathrm{CAN}})$ plane, which we discuss further in Section 7.

6.1 From I to II and from II to VI

The transitions from region I to II and from region II to VI are well understood when $g_{\mathrm{CAN}} = 0$ (Best et al. 2005). The transition mechanisms persist when $g_{\mathrm{CAN}} > 0$. Starting from region I, an increase in g_{NaP} pushes hp_{SN} low enough that the hp-nullcline no longer intersects the family of quiescent critical points, and $F(Ca, Na, hp, x_0) = P(Ca, Na, hp)$ once $hp > hp_{SN}$. This change in the location of the intersection point provides the transition from region I to region II. In the transition from region II to region VI, a further increase in g_{NaP} moves the homoclinic surface enough such that the net drift of hp along the homoclinic is nonnegative, such that hp can never lead the transition back to the silent phase and tonic spiking is attained.

6.2 From II to *

The transition from region II to region * is similar to the transition from region II to region VI. The key point is that in region II, the CAN current does not sufficiently activate to take control of the active phase before the decrease in hp can terminate it. With an increase in g_{NaP}, even without CAN current activation, the trajectory can no longer return to the silent phase simply by virtue of hp decreasing. Without a contribution from I_{CAN} the resultant solution would be tonically active, as in region VI. Such spiking activity sustains an elevated value for Ca. Even if this sustained $Ca < k_{Ca}$, and so may not be enough to activate the CAN current in the traditional sense, it may enable to the CAN current to have a slight influence on the voltage. This influence is amplified by g_{CAN}, and for g_{CAN} large enough, it qualitatively changes the dynamics by giving the trajectory the extra spike needed to fully activate the CAN current. The tipping point for this qualitative change is shown as the lower boundary for region * in Fig. 6. Thus, as described in Section 5.3, alternation of DB and square-wave bursts, depending on levels of Na ensues. Recall from Section 3.1 $D = D(hp)$ was the net drift of hp across the homoclinic orbit. In brief, in region II, $D < 0$, and it is increasing g_{NaP} such that $D = 0$, in the presence of enhanced I_{CAN}, that triggers a transition to region *.

6.3 From * to III

Increasing g_{NaP} further increases $D = D(hp)$, such that in region III, unlike region *, levels of Na attained by typical DB bursts maintain $D > 0$. While $D > 0$, the only way for a solution to return to the silent phase is through a DB burst, and thus DB bursting characterizes region III.

6.4 From III to IV

The key feature of solutions in region III is that eventually $Ca > Ca_{AH}(Na, hp)$, so that $F(Ca, Na, hp, x_0) = DB(Na, hp)$. $Ca_{AH}(Na, hp)$ is a decreasing function of g_{CAN}, see Fig. 15. As g_{CAN} decreases, $Ca_{AH}(Na, hp)$ blows up for finite g_{CAN}. This blowup can be used to indicate a transition from region III to region IV, because for lower g_{CAN} the system cannot go into depolarization block. In Fig. 19, we plot the predicted boundary between regions III and IV, based on where this blowup occurs. To determine the value of g_{CAN} such that $Ca_{AH}(Na, hp)$ blows up, we must fix Na and hp. We fixed Na at 6.5, a value higher than those normally seen in bursting activity, but lower than is seen in tonic activity. We also set $hp = 0$, assuming a prolonged active phase. For each value of g_{NaP}, we found g_{CAN} such that $Ca_{AH}(Na, hp) = 1.6$, a typical saturation value for Ca during tonic activity. This scheme gives us the red boundary curve seen in Fig. 19.

Similarly, $I_{\mathrm{NaP}}(v, hp)$ is a depolarizing current, so $Ca_{AH}(Na, hp)$ is a decreasing function of g_{NaP} as well. This means that an increase in g_{NaP} decreases $Ca_{AH}(Na, hp)$, so that we need a slightly lower g_{CAN} to maintain $Ca_{AH}(Na, hp) = 1.6$. This relationship causes the negative slope of the boundary between regions III and IV.

6.5 From IV to V and V to VI

In Fig. 20, we present an approximation to the boundary between regions IV and V and to the boundary between regions V and VI. These approximations are not based on a slow-fast decomposition, but rather on a bifurcation analysis of the full system. To find these curves, we start with a tonic solution T in region IV and follow T as g_{CAN} is decreased, with g_{NaP} fixed. T loses stability at a torus, or Neimark-Sacker, bifurcation; we color the $(g_{\mathrm{NaP}}, g_{\mathrm{CAN}})$ at which the torus bifurcation occurs magenta. We continue to follow T until it regains stability at another torus bifurcation, coloring the corresponding bifurcation point blue. We note that the continuation analysis performed in XPPAUT (Ermentrout 2002), due to the

incidence of limit point of periodic orbit (LPPO) bifurcations, is not necessarily monotonic in g_{CAN}, see Fig. 21. This lack of monotonicity occurs for low g_{NaP} so that even though the magenta point is identified first by the algorithm, the blue point occurs for higher values of g_{CAN}. The magenta curve accurately predicts the boundary between regions IV and V, while the blue curve gives an accurate estimate of the boundary between regions V and VI for sufficiently large g_{NaP} and deviates as g_{NaP} decreases (but see Section 7).

We can also predict the boundary between regions IV and V based on the slow-fast decomposition. The mechanism that distinguishes regions IV and V is that in in region V, Ca_{HC} blows up to trigger a return to the silent phase. This blow up occurs after an extended time in the active phase, so for the rest of this analysis we assume hp has decreased to a small but nonzero value. Actually, in region IV, $Ca_{HC}(Na, hp)$ blows up for finite Na, but such values of Na are not attained. Indeed, solving $\dot{Na} = 0$ for Na yields $Na_{fp}(v, Ca)$, the value that Na will approach based on the activity of the CAN current. For a given (g_{NaP}, g_{CAN}) pair, the value $Na = Na^*$ for which $Ca_{SN}(Na, hp)$ blows up may be such that $Na^* > Na_{fp}(v, Ca)$; that is, the Na dynamics will saturate at $Na_{fp}(v, Ca)$ and never reach Na^*. As such, the blow up of $Ca_{HC}(Na, hp)$ will never occur for this (g_{NaP}, g_{CAN}) pair, so we know that (g_{NaP}, g_{CAN}) belongs to region IV. On the other hand, if $Na^* < Na_{fp}(v, Ca)$, then as Na drifts toward its saturation value $Na_{fp}(v, Ca)$, it crosses Na^*, causing $Ca_{HC}(Na, hp)$ to blow up and capture the trajectory, triggering a return to the silent phase. This places (g_{NaP}, g_{CAN}) in region V. The border between IV and V therefore is the curve of (g_{NaP}, g_{CAN}) pairs where $Na^* = Na_{fp}(v, Ca)$. To approximate this border, we first allow Na^* to be the value of Na such that $Ca_{HC}(Na^*, hp) = Ca^*$ where Ca^* must be determined. As $Ca_{HC}(Na^*, hp)$ increases, the fast subsystem approaches a homoclinic orbit, and this increased time between spikes can have subtle effects on the drift for Ca and Na. We tried many values for Ca^*, and $Ca^* = 1.01$ gave the best fit for the border. We also use the fact that for low hp, $Ca_{SN}(Na, hp)$ approximates $Ca_{HC}(Na, hp)$ well. For fixed Ca we calculate the mean v, s over one period of the tonic spiking solution. Using this mean s in Eq. (5), we calculate the drift of Ca, which changes the value of the CAN current. With mean v and adjusted Ca, we calculate an approximation for $Na_{fp}(v, Ca)$. This updated Na moves the homoclinic surface, possibly changing the mean v, s for the tonic spiking solutions with updated fixed Ca. We iterate this calculation until $Na_{fp}(v, Ca)$ changes by no more than 10^{-3}, and call this value Na_{fp}. In Fig. 19 we plot in magenta the (g_{NaP}, g_{CAN}) pairs such that $Na_{fp} = Na^*$.

Again, because $I_{NaP}(v, hp)$ is a depolarizing current, a slight increase to g_{NaP} lowers Ca_{SN}, thus requiring slightly higher Na for $Ca_{SN}(Na, hp) \approx Ca_{HC}(Na, hp)$ to blow up. On the other hand, increasing g_{NaP} has little effect on $Na_{fp}(v, Ca)$. Therefore, increasing g_{NaP} from a point on the border of regions IV and V causes $Na^* > Na_{fp}$, resulting in the dynamics of region IV, consistent with the negative slope of the boundary curve between regions IV and V.

7 Bistability

Figure 20 predicts several regions of bistability. Tonic solutions where the CAN current is activated, similar to those solutions commonly seen in region IV, are found for (g_{NaP}, g_{CAN}) above the magenta curve in Fig. 20. For appropriate values of (g_{NaP}, g_{CAN}), these tonic solutions coexist with the previously described solutions of regions I, II, III, VI and *. Similarly, for (g_{NaP}, g_{CAN}) below (to the left) of the blue curve in Fig. 20, there are tonic solutions where the CAN current does not play a strong role. These solutions are like those solutions commonly found in region VI and coexist with the previously described solutions of regions *, III and IV. Such solutions lose stability at the boundary of region II and so they are not observed in regions II or I. We summarize the result of this bistability analysis in

Fig. 22. In Table 2, we list the regions of Fig. 22 together with the regions for which corresponding solutions were originally described.

8 Discussion

In this work we consider a computational model for respiratory neurons in the preBötC that includes the CAN current and the Na/K ATPase pump, as modeled in theRubin–Hayes model (Rubin et al. 2009b), and the NaP current, all of which are ubiquitous within this population of neurons. By considering varying strengths of g_{CAN}, the conductance of the CAN current, and g_{NaP}, the conductance of the NaP current, we explain the mechanisms through which the model yields dynamics seen in *in vitro* recordings, such as square-wave bursting (2 different mechanisms), bursts featuring depolarization block (DB bursts), and mixed patterns of square-wave and DB bursts, as well as tonic activity. Although analysis is done for one model neuron, the model is self-coupled, and so actually represents the activity of a small, synaptically coupled network. Using our understanding of the bifurcation structure of the fast subsystem, we compute estimates of where transitions between dynamic regimes are predicted to occur, and these agree with direct simulations, validating our analysis. We predict that activity patterns shown in this work will be observed in reciprocally coupled pairs of preBötC neurons, as well as preBötC neurons that are manipulated in culture to form autapses.

A multitude of factors influence the activation and magnitude of the CAN current in a biological setting. In the present model, activation of the CAN current depends on intracellular calcium, which is released via a synaptic pathway. Acting through AMPA receptors, glutamate can trigger a small influx of calcium (Pace and Del Negro 2008), while glutamate binding to metabotropic glutamate receptors (specifically mGluR5s) can induce G protein activation that leads to inositol 1,4,5-trisphosphate (IP_3) synthesis and subsequent intracellular calcium release. These two mechanisms work in concert to recruit the CAN current (Pace et al. 2007a; Pace and Del Negro 2008). Phosphatidyl 4,5-bisphosphate (PIP_2) is required to synthesize IP_3 and is generally abundant in preBötC neurons (Crowder et al. 2007). Levels of PIP_2 in the membrane surrounding the channels may fluctuate or be regulated and thus affect channel availability, however, which impacts the magnitude of the CAN current (Liu and Liman 2003). Finally, second messengers such as calcium can also adjust the magnitude of the CAN current by affecting the phosphorylation state of relevant ion channels (Nilius et al. 2006; Crowder et al. 2007). Given the variety of factors that could contribute to the heterogeneity in CAN current magnitude and activity across neurons in the preBötC, it was most convenient simply to use variations in the parameter g_{CAN} to represent these effects, as a means to explore how changes in the CAN current characteristics influence preBötC neuron dynamics. The characteristics of the NaP current within the preBötC also exhibit inherent biological variability, which we represent in this work by modulating g_{NaP}.

Rhythmic activity in the preBötC can be influenced by either the NaP current or the CAN current, as shown previously (Butera et al. 1999a; Rubin et al. 2009b), but their combination in this paper gives a spectrum of additional activity patterns and bistability that are expected to arise in the preBötC network. In particular, alternation of square-wave and DB bursts is seen in experimental data, and is often attributed to intrinsic noise and neuronal variability, but our unified model suggests that such bursting may result from the interactions of the CAN and NaP currents. DB bursts require activation of the CAN current, which also increases Na so that the Na/K ATPase pump leads to eventual burst termination. Although Na decays during the subsequent silent phase, Na may be elevated enough during the next burst that the Na/K ATPase pump and NaP inactivation together may terminate the burst before the CAN current is activated. This interaction may cause one or more square-wave

bursts to occur between DB bursts and can also be used to explain the differences in durations of the silent phases between such bursts. Specifically, we observed in our sample of *in vitro* recordings that, in a preBötC neuron that has both DB and square-wave bursts, the silent phase following a DB burst was generally longer than the silent phase following a square-wave burst (Fig. 14). We explained this phenomenon by noting that after a DB burst, the Na/K ATPase pump experiences an increased load, which prolongs the silent phase by requiring more NaP deinactivation to occur before the next burst can start. During a subsequent square-wave burst, as noted above, the load on the pump decreases, resulting in a shorter silent phase before NaP deinactivation initiates the next burst. Thus, the model predicts that this link between the nature of a burst and the duration of the subsequent interburst interval should be a general feature of activity of the type generated by the unified model for parameter values from region *.

In addition to underlying square-wave bursting, to contributing to the mixed burst patterns seen in region * and prevalent in electrophysiological recordings (Fig. 8), and to helping control interburst interval durations, the NaP current plays a role in boosting synaptic activation, due to its voltage-dependence. In the unified model, this boost can promote DB bursts if both g_{NaP} and g_{CAN} are large enough. By increasing the spike rate during tonic activity, the NaP current can contribute to CAN current activation, resulting in a transition through depolarization block and eventually a return to quiescence. Indeed, increasing g_{NaP} increases the range of g_{CAN} for which DB bursting occurs (Fig. 6), which represents another model prediction.

The efforts of Rybak et al. have refined models of the NaP current (Rybak et al. 2003, 2004). We expect that including such refinements would induce some quantitative differences in the locations of the boundaries between regions in Fig. 6; however, it is unlikely that these relatively minor changes would alter the qualitative bifurcation structures or model dynamics that we have described and analyzed. Toporikova and Butera recently developed a two compartment model including the CAN and NaP currents (Toporikova and Butera 2010). Their work focuses on individual model neurons that utilize either NaP inactivation, IP_3 desensitization, or a combination of these mechanisms to burst in the absence of synaptic input. In this paper, we present a recent experimental result (Fig. 1) demonstrating that, despite the lack of information regarding the distribution of the NaP and CAN currents, preBötC neurons appear to be electrotonically compact. Given this finding, and the absence of evidence that more compartments are needed to capture the essential mechanisms of burst generation, we here consider the unified model as a one compartment model. Furthermore, intrinsic rhythmicity in individual preBötC neurons is neither necessary for preBötC rhythmicity (Del Negro et al. 2002b, 2005) nor necessarily advantageous for burst synchrony over a broad parameter range (Dunmyre and Rubin 2010), and our unified model highlights the diversity of burst-generation mechanisms that emerge through the interaction of synaptically-gated channels with other voltage-dependent channels. It is possible that including desensitization of IP_3 in the unified model may alter the locations and burst frequencies associated with regions * and III of Fig. 6 by delaying activation of the CAN current or yielding earlier burst termination with less Na accumulation, and these effects should be explored in future work. We also note that E_L, the reversal potential of the leak current, has been focused on in previous modeling work on the preBötC because it can significantly impact certain forms of model dynamics, it can be manipulated experimentally through alterations in potassium concentrations external to neurons, and it can serve as a proxy for variations in I_{app} (since $g_L E_L$ and I_{app} play identical roles) (Butera et al. 1999a; Rubin and Terman 2002; Rubin et al. 2009b). If E_L is perturbed, then similar forms of dynamics to those seen in Fig. 6 arise, albeit with differences in region locations. Larger increases in E_L can push the model away from bursting toward tonic spiking, although DB bursts persist for sufficiently high g_{CAN} until they are transformed into elliptic-like bursts

due to the failure of the Na/K ATPase pump to create a prolonged silent phase, as discussed in Section 4.

While our work is motivated by the dynamics observed in the preBötC (e.g. Fig. 8), it may be applicable to other rhythmic brain areas as well. In many mammalian locomotor CPGs, the NaP current has been identified as playing a critical role in generating the network rhythm (Tazerart et al. 2007, 2008; Zhong et al. 2007). On the other hand, in other rhythmic brain areas such as entorhinal cortex (Egorov et al. 2002; Fransén et al. 2006) or the trigeminal system (Tsuruyama et al. 2008), the CAN current plays a critical role in pattern generation. In fact, the trigeminal system features both NaP (Wu et al. 2005) and CAN currents. Indeed, given that CAN and NaP currents are widespread and can robustly drive the array of rhythmic activity patterns presented and analyzed in this paper, it seems likely that the interaction of these currents is a fundamental component of neuronal rhythmogenesis. Therefore, the generalizable modeling framework that incorporates the CAN and NaP currents presented in this specific preBötC model could be useful for adaptation or application to other neuronal systems as well.

Supplementary Material

Refer to Web version on PubMed Central for supplementary material.

Acknowledgments

We thank John Hayes for assistance in collecting experimental data. This work was partially supported by National Science Foundation awards DMS-0716936, DMS-1021701 and EMSW21-RTG 0739261, and National Institute of Health grants 1R01HL104127-01 and 1R21NS070056-01.

References

Best J, Borisyuk A, Rubin J, Terman D, Wechselberger M. The dynamic range of bursting in a model respiratory pacemaker network. SIAM Journal on Applied Dynamical Systems. 2005; 4(4):1107–1139.

Brockhaus J, Ballanyi K. Synaptic inhibition in the isolated respiratory network of neonatal rats. European Journal of Neuroscience. 1998; 10(12):3823–3839. [PubMed: 9875360]

Butera R, Rinzel J, Smith J. Models of respiratory rhythm generation in the pre-Botzinger complex. I. Bursting pacemaker neurons. Journal of Neurophysiology. 1999a; 82(1):382–397. [PubMed: 10400966]

Butera R, Rinzel J, Smith J. Models of respiratory rhythm generation in the pre-Botzinger complex. II. Populations of coupled pacemaker neurons. Journal of Neurophysiology. 1999b; 82(1):398–415. [PubMed: 10400967]

Crowder E, Saha M, Pace R, Zhang H, Prestwich G, Del Negro C. Phosphatidylinositol 4, 5-bisphosphate regulates inspiratory burst activity in the neonatal mouse preBötzinger complex. The Journal of Physiology. 2007; 582(3):1047–1058. [PubMed: 17599963]

Del Negro C, Hayes J, Rekling J. Dendritic calcium activity in preBötzinger complex neurons in neonatal mice studied *in vitro*. Journal of Neuroscience. 2010 (in press).

Del Negro C, Johnson S, Butera R, Smith J. Models of respiratory rhythm generation in the pre-Botzinger complex. III. Experimental tests of model predictions. Journal of Neurophysiology. 2001; 86(1):59–74. [PubMed: 11431488]

Del Negro C, Koshiya N, Butera R Jr, Smith J. Persistent sodium current, membrane properties and bursting behavior of pre-botzinger complex inspiratory neurons in vitro. Journal of Neurophysiology. 2002a; 88(5):2242–2250. [PubMed: 12424266]

Del Negro C, Morgado-Valle C, Feldman J. Respiratory rhythm: An emergent network property? Neuron. 2002b; 34(5):821–830. [PubMed: 12062027]

Del Negro C, Morgado-Valle C, Hayes J, Mackay D, Pace R, Crowder E, et al. Sodium and calcium current-mediated pacemaker neurons and respiratory rhythm generation. Journal of Neuroscience. 2005; 25(2):446–453. [PubMed: 15647488]

Dhooge A, Govaerts W, Kuznetsov Y. MATCONT: A MATLAB package for numerical bifurcation analysis of O.D.E.s. ACM Transactions on Mathematical Software (TOMS). 2003; 29(2):164.

Dunmyre JR, Rubin JE. Optimal intrinsic dynamics for bursting in a three-cell network. SIAM Journal on Applied Dynamical Systems. 2010; 9:154–187. http://link.aip.org/link/?SJA/9/154/1.

Egorov A, Hamam B, Fransén E, Hasselmo M, Alonso A. Graded persistent activity in entorhinal cortex neurons. Nature. 2002; 420(6912):173–178. [PubMed: 12432392]

Ermentrout, G. Simulating, analyzing, and animating dynamical systems: A guide to XPPAUT for researchers and students. Society for Industrial Mathematics; 2002.

Feldman J, Del Negro C. Looking for inspiration: New perspectives on respiratory rhythm. Nature Reviews Neuroscience. 2006; 7(3):232–241.

Feldman J, Smith J. Cellular mechanisms underlying modulation of breathing pattern in mammals. Annals of the New York Academy of Sciences. 1989; 563:114–130. (Modulation of Defined Vertebrate Neural Circuits). [PubMed: 2476055]

Fenichel N. Geometric singular perturbation theory for ordinary differential equations. Journal of Differential Equations. 1979; 31(1):53–98. http://www.sciencedirect.com/science/article/B6WJ2-4KF75DG-5/%2/759c4cfb4dfa51704c3b8edb0e864f48.

Fransén E, Tahvildari B, Egorov A, Hasselmo M, Alonso A. Mechanism of graded persistent cellular activity of entorhinal cortex layer v neurons. Neuron. 2006; 49(5):735–746. [PubMed: 16504948]

Hindmarsh A, Brown P, Grant K, Lee S, Serban R, Shumaker D, et al. SUNDIALS: Suite of nonlinear and differential/algebraic equation solvers. ACM Transactions on Mathematical Software (TOMS). 2005; 31(3):363–396.

Jones C. Geometric singular perturbation theory. Dynamical Systems (Montecatini Terme 1994). 1994; 1609:44–118.

Koizumi H, Smith J. Persistent Na+ and K+-dominated leak currents contribute to respiratory rhythm generation in the pre-Botzinger complex in vitro. Journal of Neuroscience. 2008; 28(7):1773–1785. [PubMed: 18272697]

Lee R, Heckman C. Essential role of a fast persistent inward current in action potential initiation and control of rhythmic firing. Journal of Neurophysiology. 2001; 85(1):472–427. [PubMed: 11152749]

Liu D, Liman E. Intracellular Ca2+ and the phospholipid P.I.P.2 regulate the taste transduction ion channel TRPM5. Proceedings of the National Academy of Sciences of the United States of America. 2003; 100(25):15160–15165. [PubMed: 14657398]

Mironov S. Metabotropic glutamate receptors activate dendritic calcium waves and TRPM channels which drive rhythmic respiratory patterns in mice. The Journal of Physiology. 2008; 586(9):2277–2291. [PubMed: 18308826]

Morgado-Valle C, Beltran-Parrazal L, DiFranco M, Vergara J, Feldman J. Somatic Ca2+ transients do not contribute to inspiratory drive in preBötzinger complex neurons. The Journal of Physiology. 2008; 586(18):4531. [PubMed: 18635649]

Nilius B, Mahieu F, Prenen J, Janssens A, Owsianik G, Vennekens R. The Ca2+-activated cation channel TRPM4 is regulated by phosphatidylinositol 4, 5-biphosphate. The EMBO Journal. 2006; 25(3):467–478. [PubMed: 16424899]

Pace R, Del Negro C. A.M.P.A. and metabotropic glutamate receptors cooperatively generate inspiratory-like depolarization in mouse respiratory neurons in vitro. European Journal of Neuroscience. 2008; 28(12):2434–2442. [PubMed: 19032588]

Pace R, Mackay D, Feldman J, Del Negro C. Inspiratory bursts in the preBötzinger complex depend on a calcium-activated non-specific cation current linked to glutamate receptors in neonatal mice. The Journal of Physiology. 2007a; 582(1):113–125. [PubMed: 17446214]

Pace R, Mackay D, Feldman J, Del Negro C. Role of persistent sodium current in mouse preBötzinger complex neurons and respiratory rhythm generation. The Journal of Physiology. 2007b; 580(2):485–496. [PubMed: 17272351]

Paton J, Abdala A, Koizumi H, Smith J, St-John W. Respiratory rhythm generation during gasping depends on persistent sodium current. Nature Neuroscience. 2006; 9(3):311–313.

Ptak K, Zummo G, Alheid G, Tkatch T, Surmeier D, McCrimmon D. Sodium currents in medullary neurons isolated from the pre-Botzinger complex region. Journal of Neuroscience. 2005; 25(21): 5159–5170. [PubMed: 15917456]

Purvis LK, Smith JC, Koizumi H, Butera RJ. Intrinsic bursters increase the robustness of rhythm generation in an excitatory network. Journal of Neurophysiology. 2007; 97(2):1515–1526. http://jn.physiology.org/cgi/content/abstract/97/2/1515, http://jn.physiology.org/cgi/reprint/97/2/1515.pdf. [PubMed: 17167061]

Ren J, Greer J. Modulation of respiratory rhythmogenesis by chloride-mediated conductances during the perinatal period. Journal of Neuroscience. 2006; 26(14):3721–3730. [PubMed: 16597726]

Rubin J, Terman D. Synchronized activity and loss of synchrony among heterogeneous conditional oscillators. SIAM Journal on Applied Dynamical Systems. 2002; 1(1):146–174.

Rubin J, Shevtsova N, Ermentrout B, Smith J, Rybak I. Multiple rhythmic states in a model of the respiratory cpg. Journal of Neurophysiology. 2009a; 101:2146–2165. [PubMed: 19193773]

Rubin JE. Bursting induced by excitatory synaptic coupling in nonidentical conditional relaxation oscillators or square-wave bursters. Physical Review E. (Statistical, Nonlinear, and Soft Matter Physics). 2006; 74(2) 021917 http://link.aps.org/abstract/PRE/v74/e021917.

Rubin JE, Hayes J, Mendenhall J, Del Negro C. Calcium-activated nonspecific cation current and synaptic depression promote network-dependent burst oscillations. Proceedings of the National Academy of Sciences. 2009b; 106(8):2939–2944. http://www.pnas.org/content/106/8/2939.abstract, http://www.pnas.org/content/106/8/2939.full.pdf+html.

Rybak I, Abdala A, Markin S, Paton J, Smith J. Spatial organization and state-dependent mechanisms for respiratory rhythm and pattern generation. Progress in Brain Research. 2007; 165:201–220. [PubMed: 17925248]

Rybak I, Shevtsova N, St-John W, Paton J, Pierrefiche O. Endogenous rhythm generation in the pre-Botzinger complex and ionic currents: Modelling and *in vitro* studies. European Journal of Neuroscience. 2003; 18(2):239–257. [PubMed: 12887406]

Rybak I, Shevtsova N, Ptak K, McCrimmon D. Intrinsic bursting activity in the pre-Botzinger complex: Role of persistent sodium and potassium currents. Biological Cybernetics. 2004; 90(1): 59–74. [PubMed: 14762725]

Shao X, Feldman J. Respiratory rhythm generation and inhibition of expiratory neurons in pre-Botzinger complex: Differential roles of glycinergic and G.A.B.A.ergic neuronal transmission. Journal of Neurophysiology. 1997; 77:1853–1860. [PubMed: 9114241]

Smith J, Abdala A, Koizumi H, Rybak I, Paton J. Spatial and functional architecture of the mammalian brainstem respiratory network: A hierarchy of three oscillatory mechanisms. Journal of Neurophysiology. 2007; 98:3370–3387. [PubMed: 17913982]

Smith J, Ellenberger H, Ballanyi K, Richter D, Feldman J. Pre-Botzinger complex: A brainstem region that may generate respiratory rhythm in mammals. Science. 1991; 254(5032):726. [PubMed: 1683005]

Tazerart S, Viemari J, Darbon P, Vinay L, Brocard F. Contribution of persistent sodium current to locomotor pattern generation in neonatal rats. Journal of Neurophysiology. 2007; 98(2):613–628. [PubMed: 17567773]

Tazerart S, Vinay L, Brocard F. The persistent sodium current generates pacemaker activities in the central pattern generator for locomotion and regulates the locomotor rhythm. Journal of Neuroscience. 2008; 28(34):8577–8589. [PubMed: 18716217]

Toporikova N, Butera R. Two types of independent bursting mechanisms in inspiratory neurons: An integrative model. Journal of Computational Neuroscience. 2010:1–14.

Tsuruyama, K.; Hsiao, C-F.; Nguyen, VT.; Chandler, SH. Intracellular calcium signaling modulates rhythmical burst activity in rat trigeminal principal sensory neurons. Program No. 575.17. 2008 Neuroscience Meeting Planner. Washington, DC: Society for Neuroscience; 2008.

Wu N, Enomoto A, Tanaka S, Hsiao C, Nykamp D, Izhikevich E, et al. Persistent sodium currents in mesencephalic v neurons participate in burst generation and control of membrane excitability. Journal of Neurophysiology. 2005; 93(5):2710–2722. [PubMed: 15625100]

Zhong G, Masino M, Harris-Warrick R. Persistent sodium currents participate in fictive locomotion generation in neonatal mouse spinal cord. Journal of Neuroscience. 2007; 27(17):4507–4518. [PubMed: 17460064]

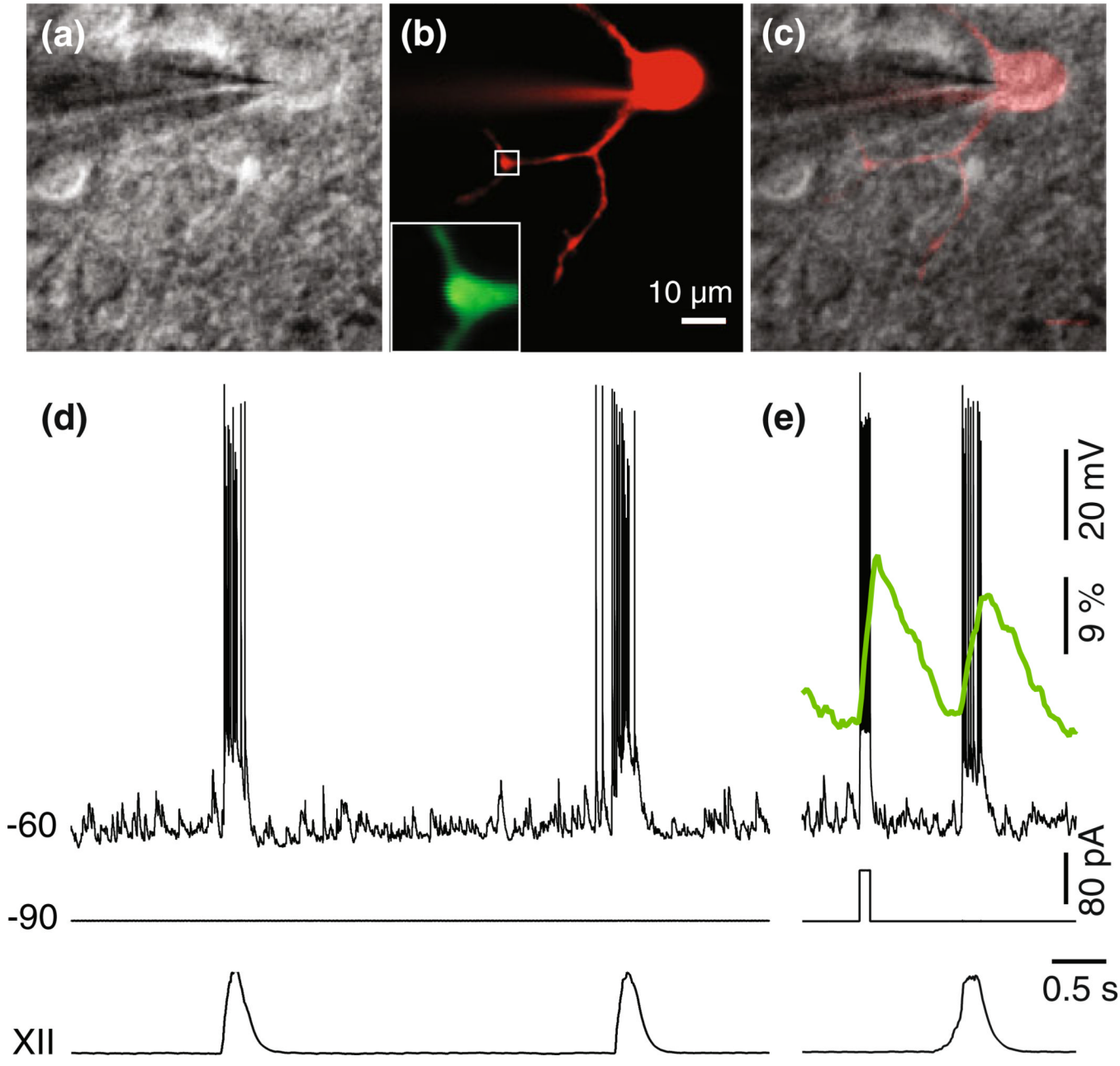

Fig. 1.

Neurons in the preBötC are electrotonically compact. (**a**) Videomicroscopic image of a whole-cell patch-clamp recording in the preBötC of a neonatal mouse. (**b**) Neuronal soma and dendrites imaged via Alexa 568 hydrazide (fast diffusing) fluorescent dye. The *white box* in (**b**) shows the dendrite region subsequently imaged using Oregon–Green BAPTA 2, a calcium-sensitive dye, and two-photon excitation (Del Negro et al. 2010). The *inset* shows this dendrite region imaged via Oregon–Green BAPTA 2. (**c**) Superimposition of (**a**) and (**b**). (**d**) Inspiratory bursts recorded immediately after achieving a whole-cell recording in the neuron (**a**)–(**c**). A bias current of −90 pA was applied to maintain a −60 mV baseline membrane potential. At first, the Alexa dye quickly dialyzes the cell (panel (**b**)) to reveal its full morphology. However, the Oregon–Green dye diffuses more slowly and does not reach the dendrite until 20–30 min later. (**e**) Whole-cell recording and dendritic imaging after 30

min. A 300 ms current step command is also illustrated to show that calcium fluorescence changes in the dendrite occur closely in time with somatic voltage changes

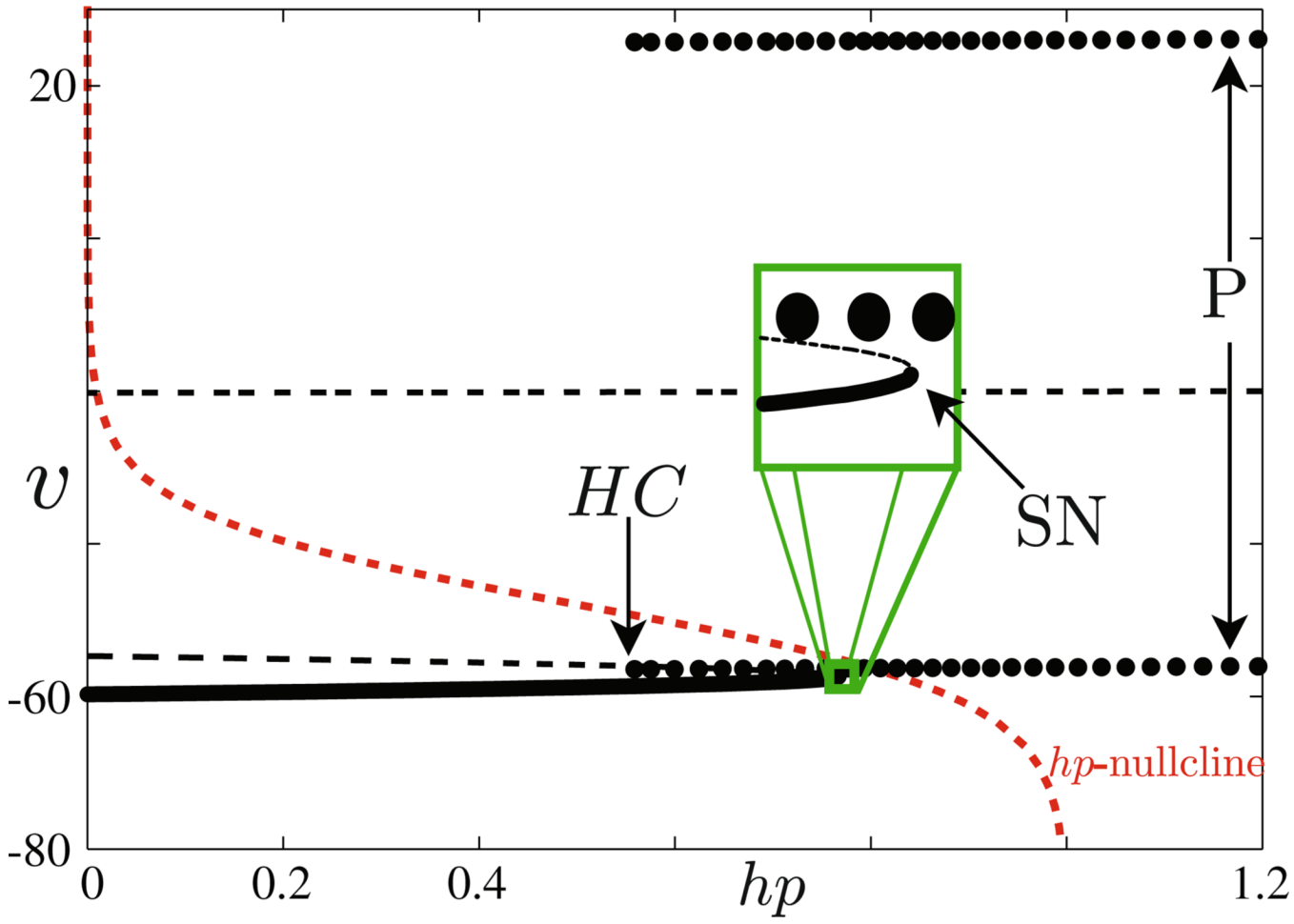

Fig. 2.

Bifurcation diagram for $g_{CAN} = 0$ formed by treating *hp* as a bifurcation parameter. *P* is a family of stable periodic orbits, the maximum and minimum *v* values of the periodic orbits are indicated by solid black circles. *P* terminates in a homoclinic orbit with homoclinic point HC. *Solid lines* indicate stable critical points, while *black dashed lines* are unstable critical points, and the sigmoidal *red dashed curve* is the *hp*-nullcline

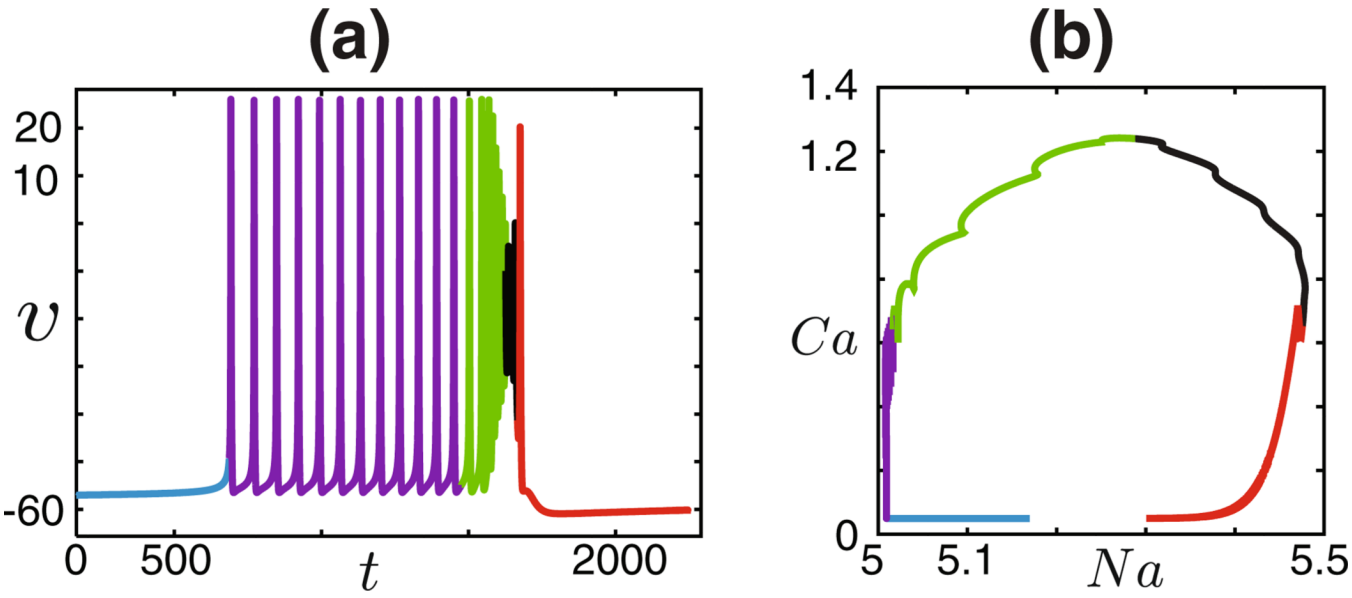

Fig. 3.

Sample trajectory for a burst in the $g_{NaP} = 0$ case. (**a**) Voltage trace. The colors correspond to those in panel (**b**). (**b**) Projection of the trajectory into the (*Na, Ca*) plane. As the model neuron spikes (*purple*), *Ca* exhibits several sharp increases until the CAN current activates (*green*), which drives both *Ca* and *Na* to higher values, eventually leading to depolarization block (*black*) and the termination of the burst (*red*)

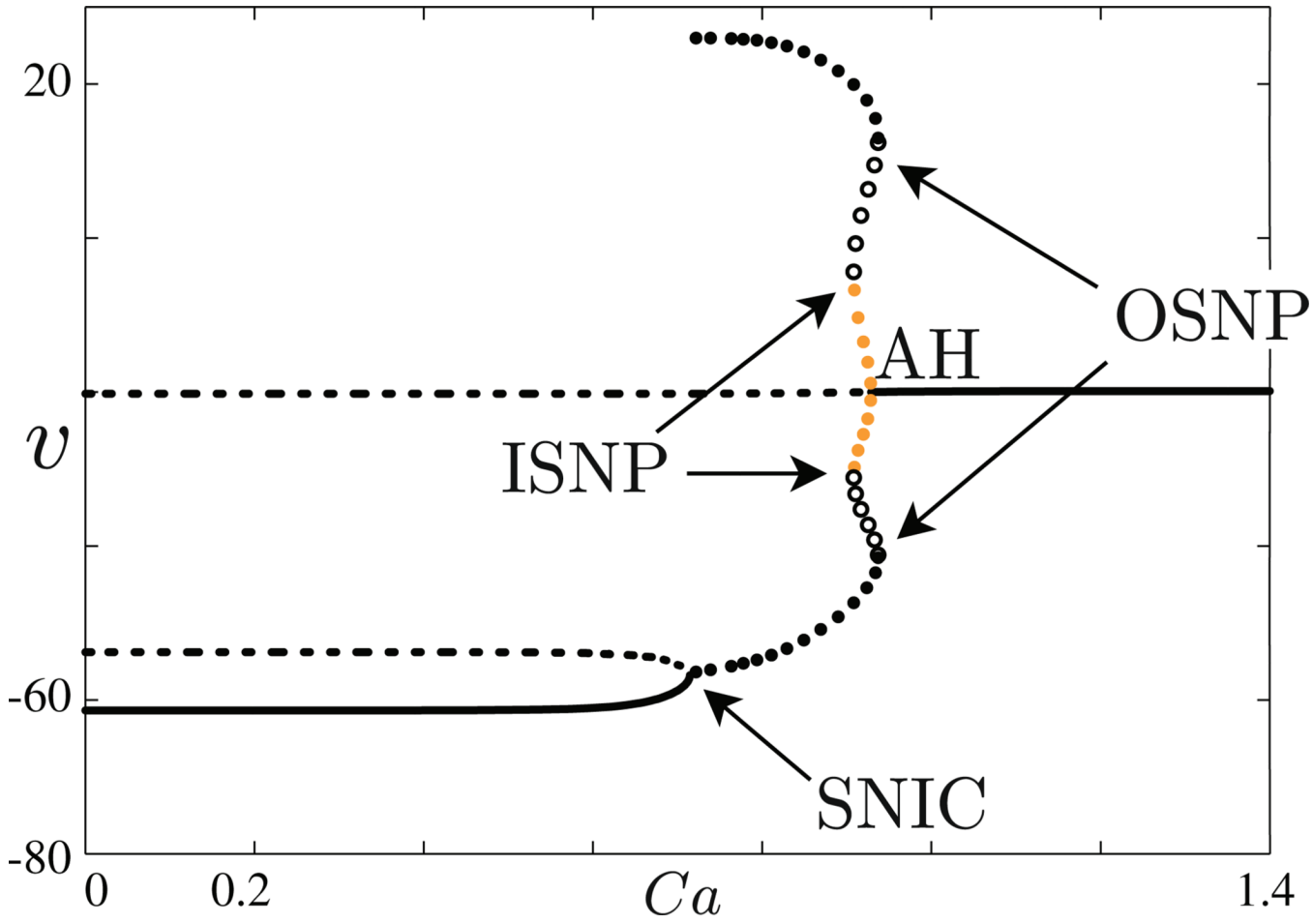

Fig. 4.

Bifurcation diagram of the fast subsystem with $g_{NaP} = 0$ generated by treating *Ca* as a bifurcation parameter. *Na* has been fixed at a level higher than Na_{base}. *Solid lines* indicate stable critical points of the fast subsystem. *Dashed lines* indicate unstable critical points of the fast subsystem. *Open* or *closed circles* mark the maximum and minimum *v* coordinates of a periodic orbit. *Closed black circles* indicate stable periodic orbits P of the fast subsystem that correspond to spiking. *Open black circles* correspond to unstable periodic orbits for the fast subsystem. *Orange circles* correspond to high voltage low amplitude oscillations L of the fast subsystem. A SN bifurcation coincides with a homoclinic bifurcation of P, resulting in a SNIC bifurcation. P meets the unstable periodic orbits at a SNP bifurcation, labeled OSNP here. The unstable periodic orbits meet L at another SNP bifurcation, labeled ISNP here. L collapses down to the branch of stable critical points corresponding to depolarization block at an AH bifurcation

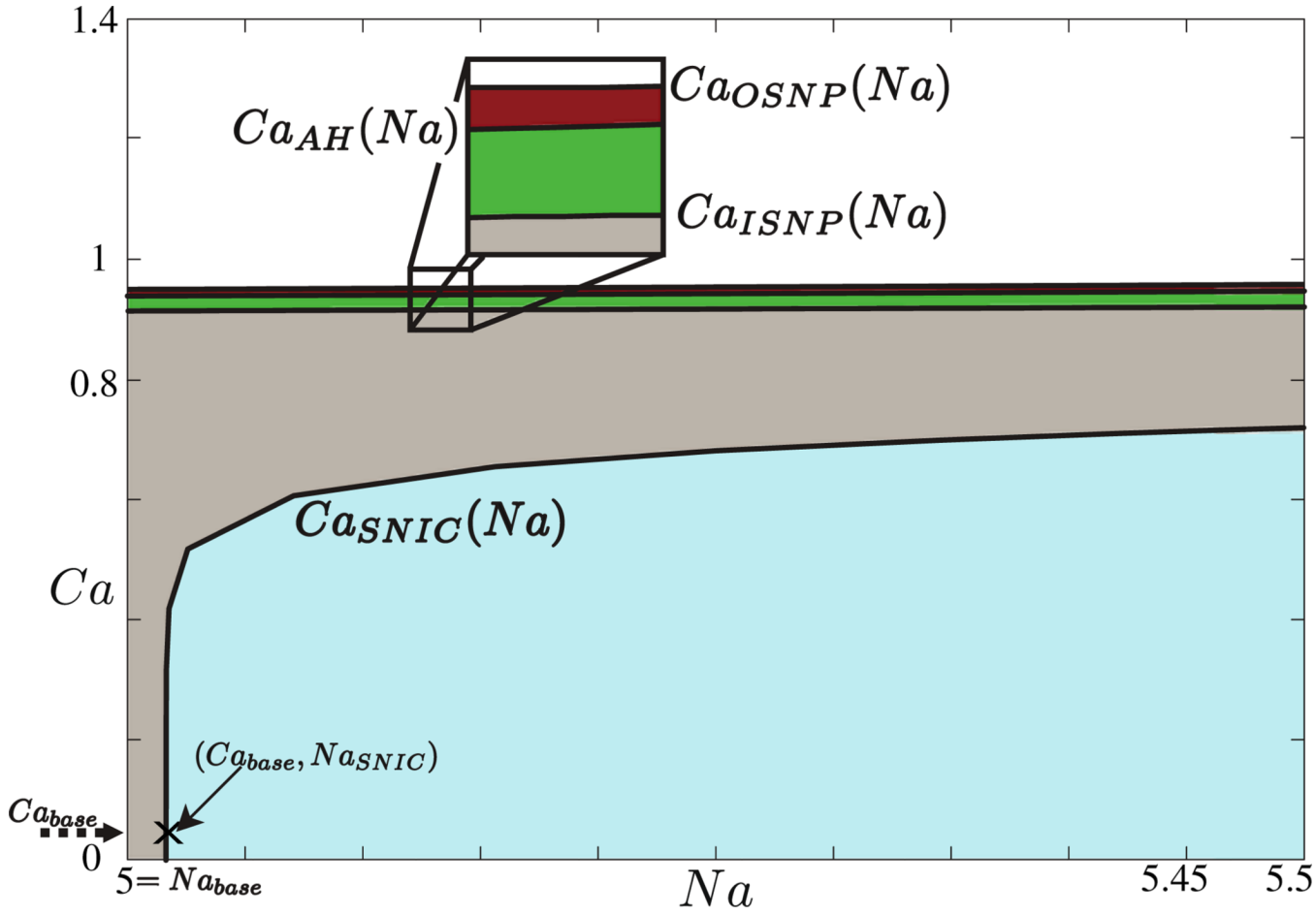

Fig. 5.

Plot of various bifurcation curves and resultant dynamics of the fast subsystem when $g_{\mathrm{NaP}} = 0$. For (*Na, Ca*) corresponding to the light blue region $F_{g_{\mathrm{NaP}}=0}(Ca, Na, x_0) = Q(Ca, Na)$. For (*Na, Ca*) corresponding to the *light grey region*, $F_{g_{\mathrm{NaP}}=0}(Ca, Na, x_0) = P(Ca, Na)$. For (*Na, Ca*) in the *green region*, there is bistability in the fast subsystem, either $F_{g_{\mathrm{NaP}}=0}(Ca, Na, x_0) = P(Ca, Na)$ or $F_{g_{\mathrm{NaP}}=0}(Ca, Na, x_0) = L(Ca, Na)$. Similarly, for (*Na, Ca*) in the *red region*, there is also bistability in the fast subsystem such that either $F_{g_{\mathrm{NaP}}=0}(Ca, Na, x_0) = P(Ca, Na)$ or $F_{g_{\mathrm{NaP}}=0}(Ca, Na, x_0) = DB(Ca, Na)$ holds. Finally, for (*Ca, Na*) in the *white region*, $F_{g_{\mathrm{NaP}}=0}(Ca, Na, x_0) = DB(Ca, Na)$. These regions are bounded by various curves of SNIC, AH, or SNP bifurcations

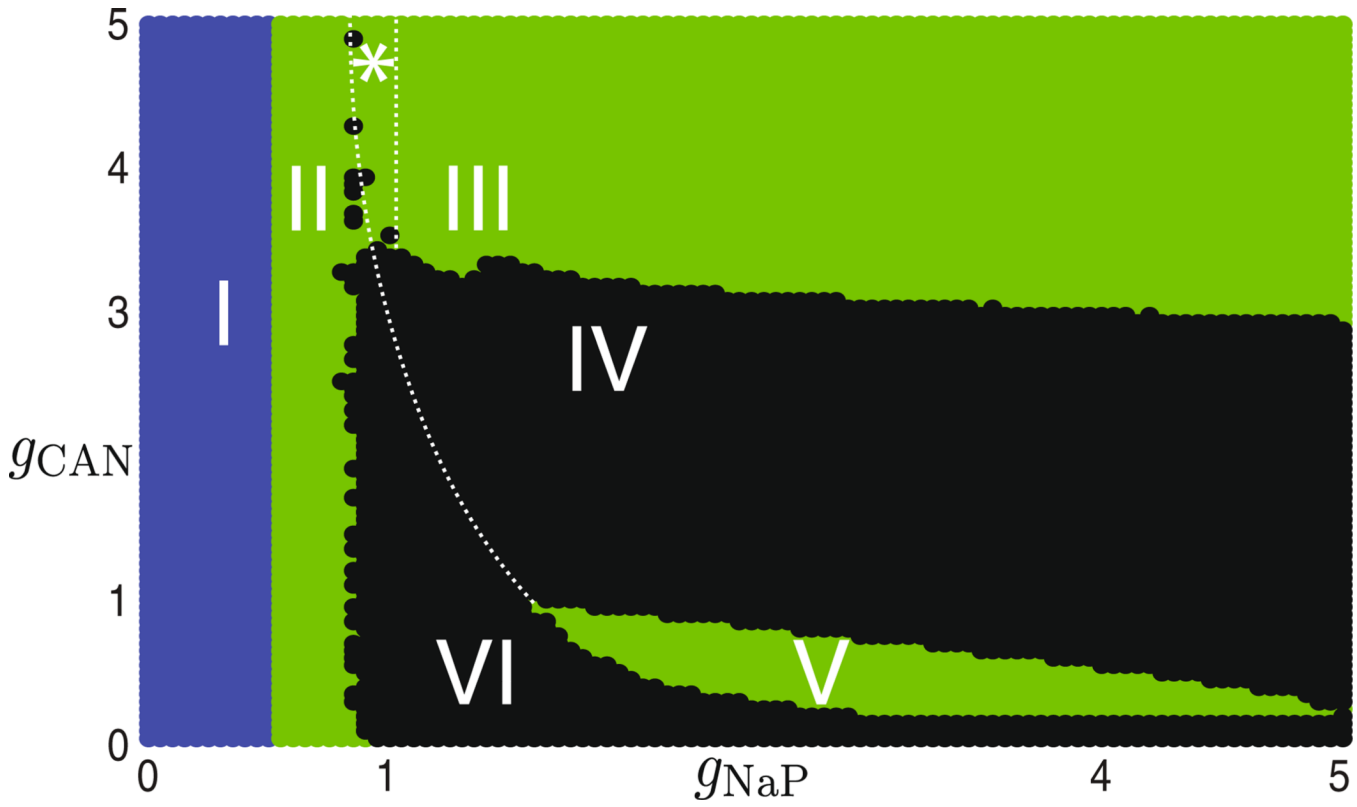

Fig. 6.

Partition of (g_{NaP}, g_{CAN}) parameter space based on the dynamics of the unified model. *Blue dots* represent quiescent solutions. *Black dots* represent tonic activity. *Green dots* represent bursting activity, either of DB bursting or square-wave bursting type. See Fig. 7 for example voltage traces corresponding to non-quiescent labeled regions

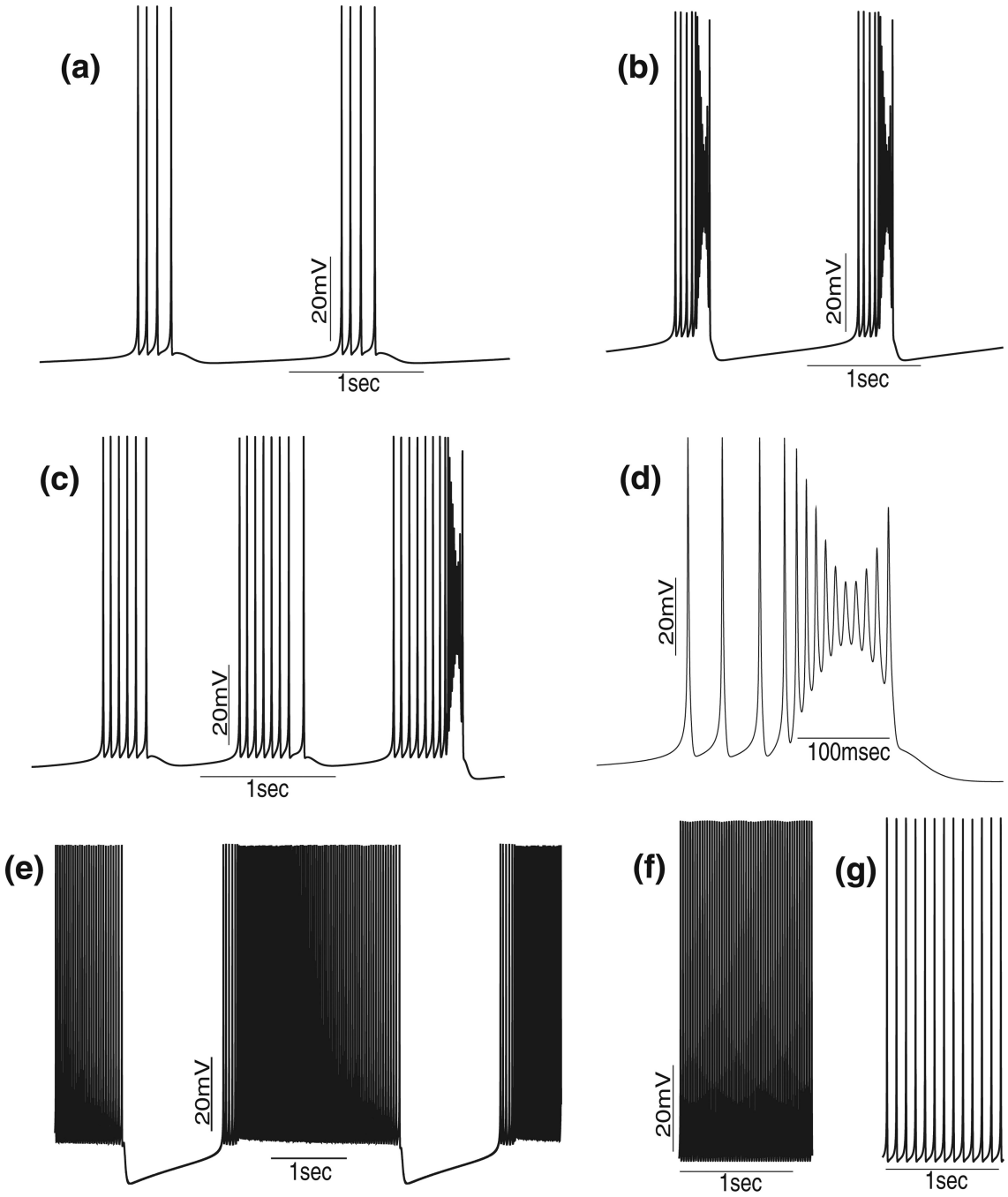

Fig. 7.

Example voltage traces of select regions from Fig. 6. Panel (**a**) corresponds to region II, (**b**) to region III, and (**c**) to region *, while panel (**d**) shows the typical structure of a DB burst from region III or region *. Panel (**e**) shows activity from region V, (**f**) from region IV, and (**g**) from region VI

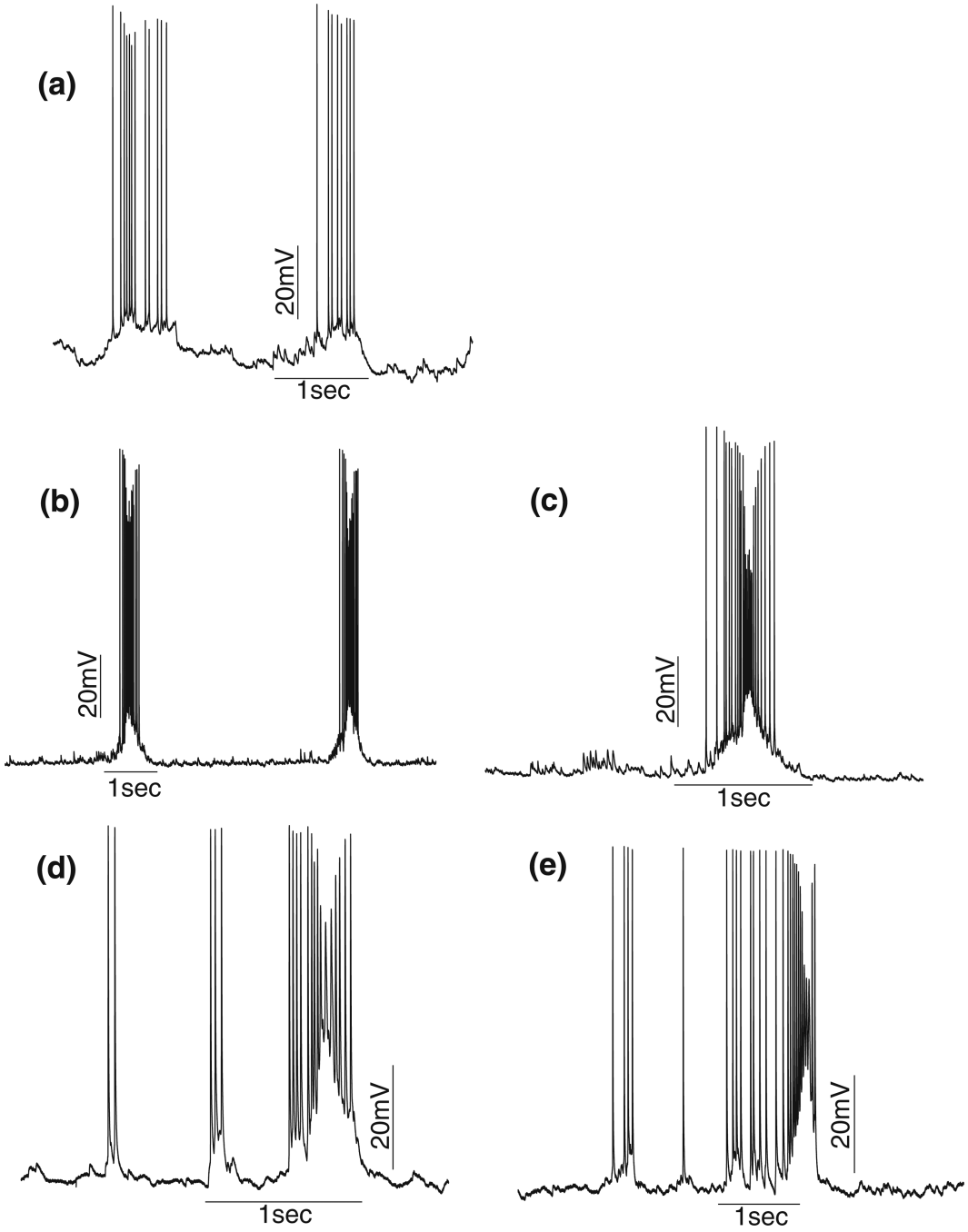

Fig. 8.

Examples from typical *in vitro* recordings from the mouse. Panel (**a**) corresponds to region II (Fig. 7(a)), panels (**b**) and (**c**) to region III (Fig. 7(b)), and panels (**d**) and (**e**) to region * (Fig. 7(c))

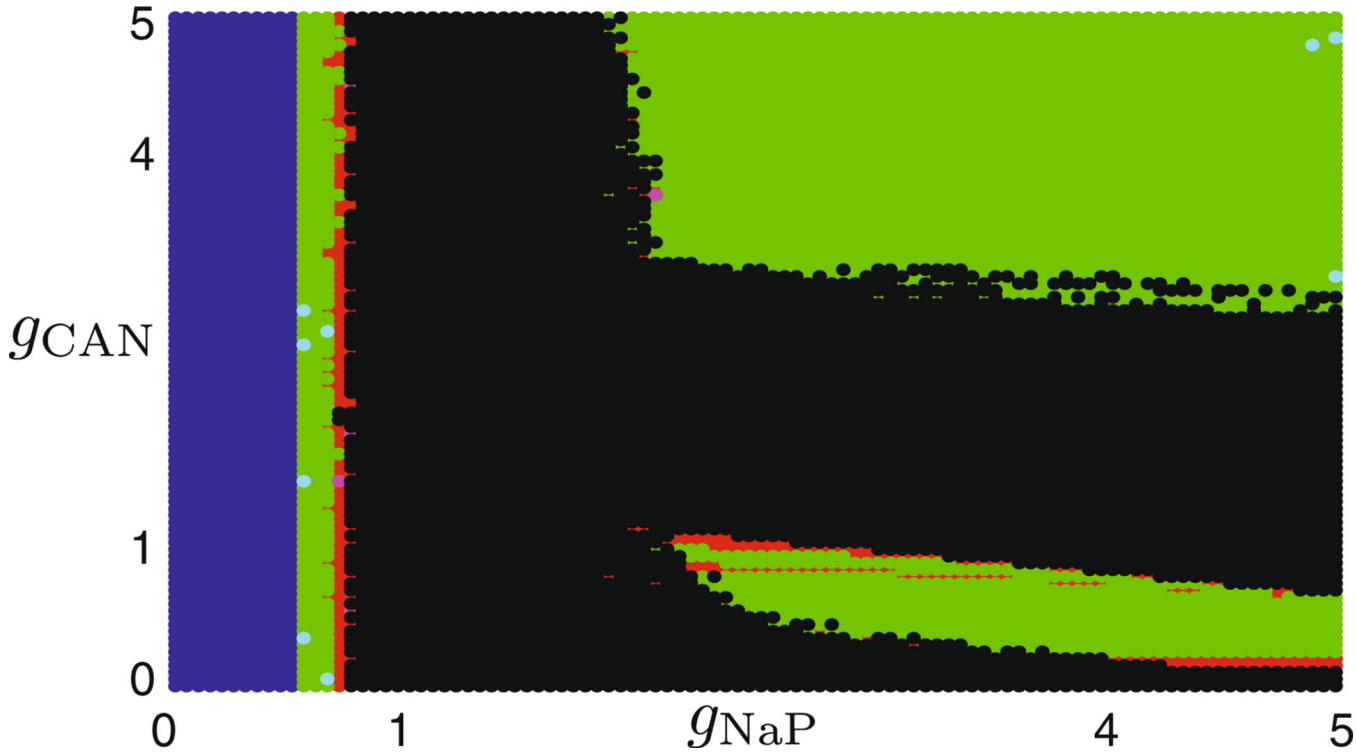

Fig. 9.

Partition of parameter space based on the dynamics of a reciprocally coupled two neuron network where each model neuron is given by the unified model without self-coupling. *Dark blue dots* represent quiescent solutions. *Black dots* represent tonic activity. *Green dots* represent in-phase DB and in-phase square-wave bursting. The relatively few ($n = 9$) occurrences of out-of-phase bursts are colored *light blue*. *Magenta dots* correspond to the rare ($n = 5$) occasion where one model neuron being identified by the algorithm as tonically active, while the other model neuron was identified as bursting. It is likely that the *magenta dots* are numerical artifacts. *Red dots* represent solutions where both model neurons were bursting based on the standard deviation of ISIs criterion, but the algorithm failed to determine the phase difference. For some values of $g_{CAN} > 3$ and $g_{NaP} > 1$ there is bistability between tonically active and bursting solutions

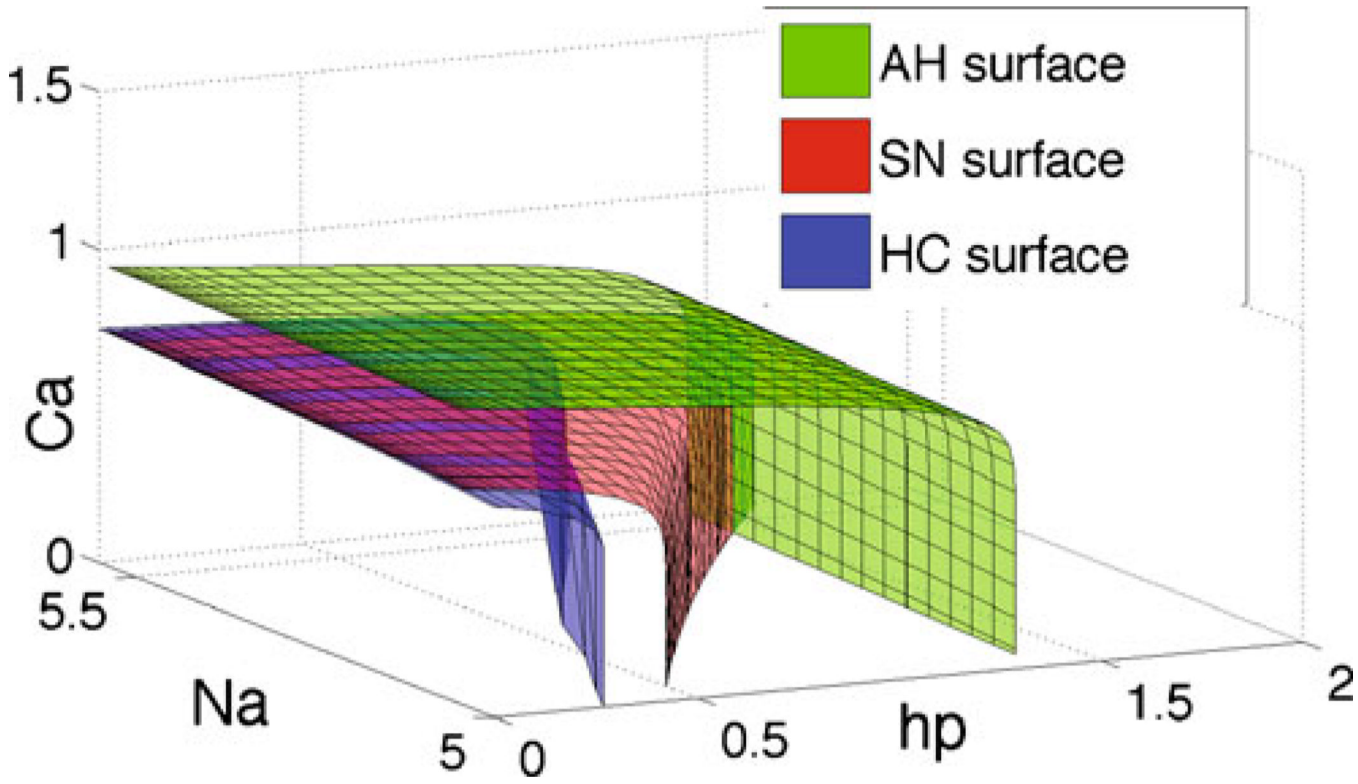

Fig. 10.

SN bifurcation surface (*red*), AH bifurcation surface (*green*), and homoclinic points (*blue*) of system (1)–(4), (8), treating *Ca, Na* and *hp* as bifurcation parameters. Notice that as *hp* decreases toward 0, the *blue* and *red* surfaces combine to form a SNIC bifurcation surface. We also note that for $Ca = 0$ and $hp = 0$, $Na_{SN} < Na_{\text{base}} = 5$, so the slow subsystem cannot pass through the SN surface unless *hp* or *Ca* increases. The MATLAB figure file is available as electronic supplementary material

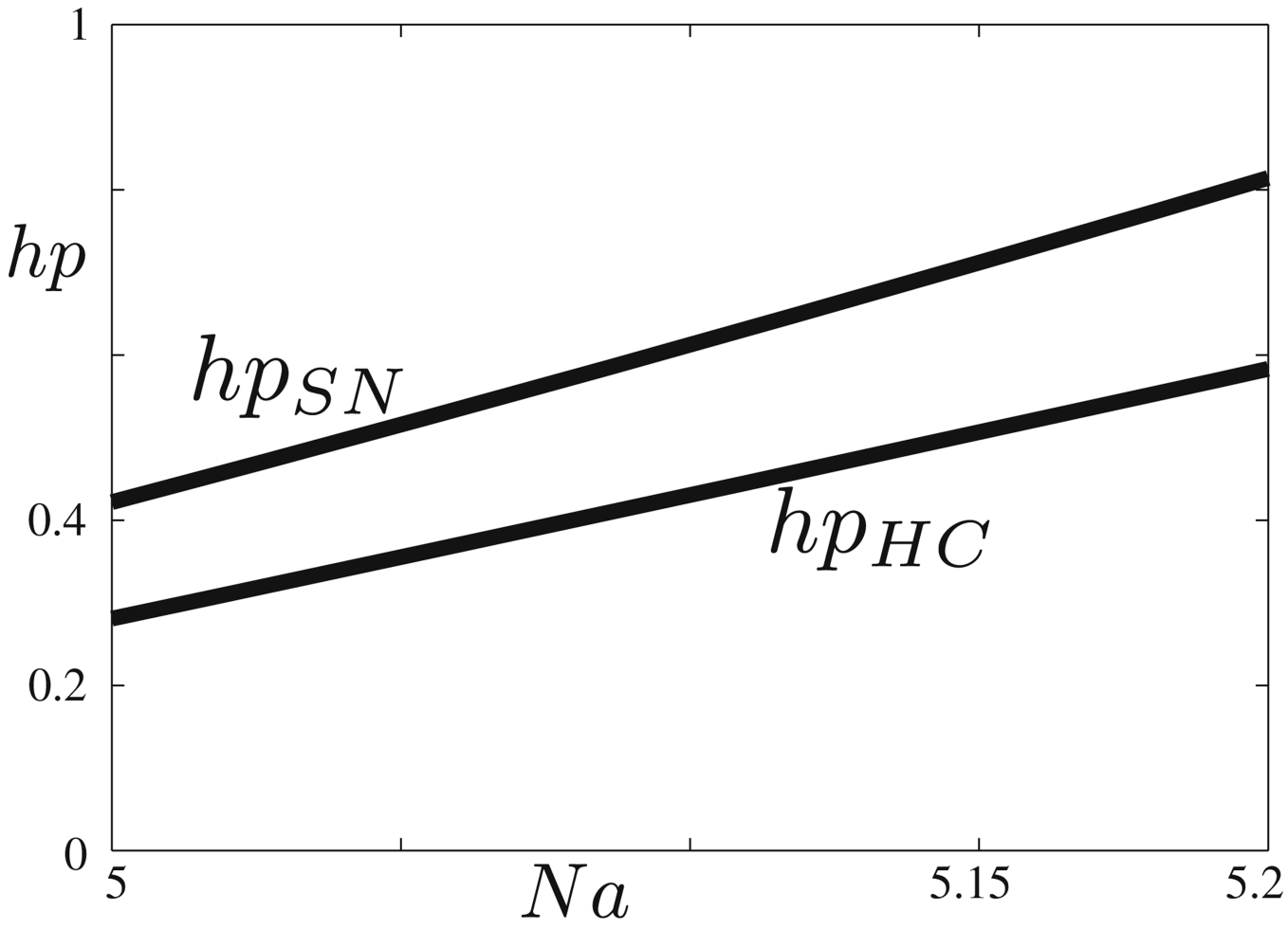

Fig. 11.

Bifurcation curves with fixed $Ca \approx Ca_{\text{base}}$. The *top curve* is hp_{SN} as a function of *Na*. The *bottom curve* is hp_{HC} as a function of *Na*. Note that the functions increase, so that a small increase in *Na* may cause hp_{HC} to be crossed, resulting in an early return to and an extended time in the silent phase

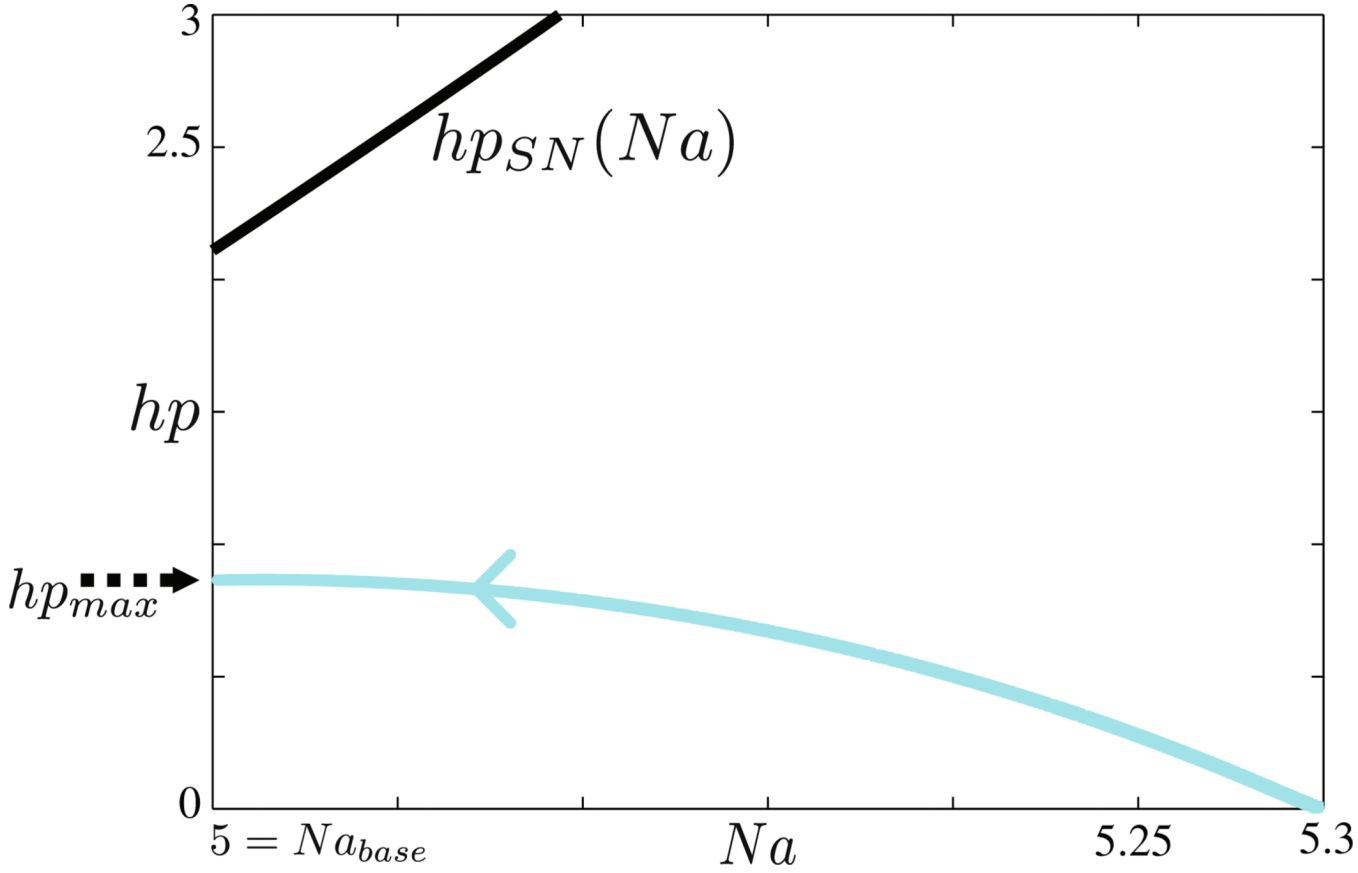

Fig. 12.

SN surface projected onto (*Ca* = Ca_{base}, *Na, hp*) coordinates is colored *black*. The *colored curve with the arrowhead* is the projection of the trajectory of the full system. The trajectory converges to (Ca_{base}, Na_{base}, hp_{max}) without crossing the SN surface, yielding a quiescent steady state

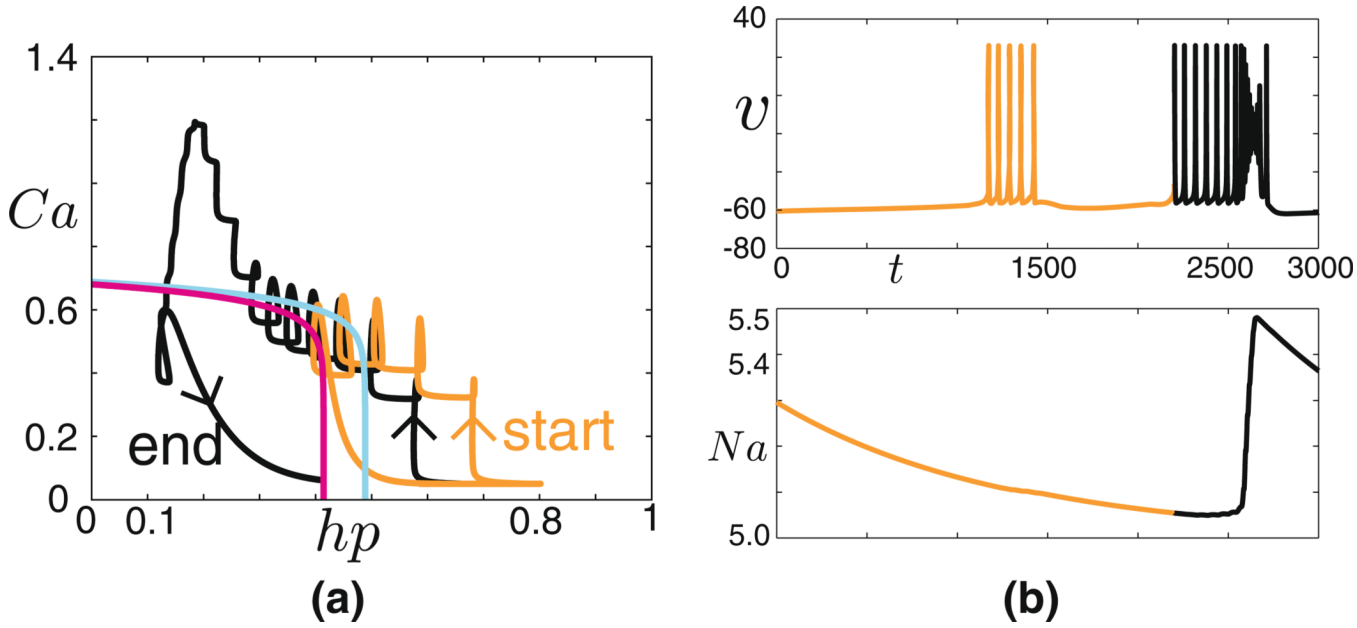

Fig. 13.

Example trajectory from region *, with projection into (*hp, Ca*) coordinates to illustrate the analysis of Section 5.4. (**a**) Projection of a trajectory from region * into (*hp, Ca*) coordinates. The *light blue curve* is a slice of the homoclinic surface for *Na* = 5.1 and the *magenta curve* is a slice of the homoclinic surface for *Na* = 5.051. (**b**) *v* and *Na* plotted against time corresponding to the trajectory in (**a**)

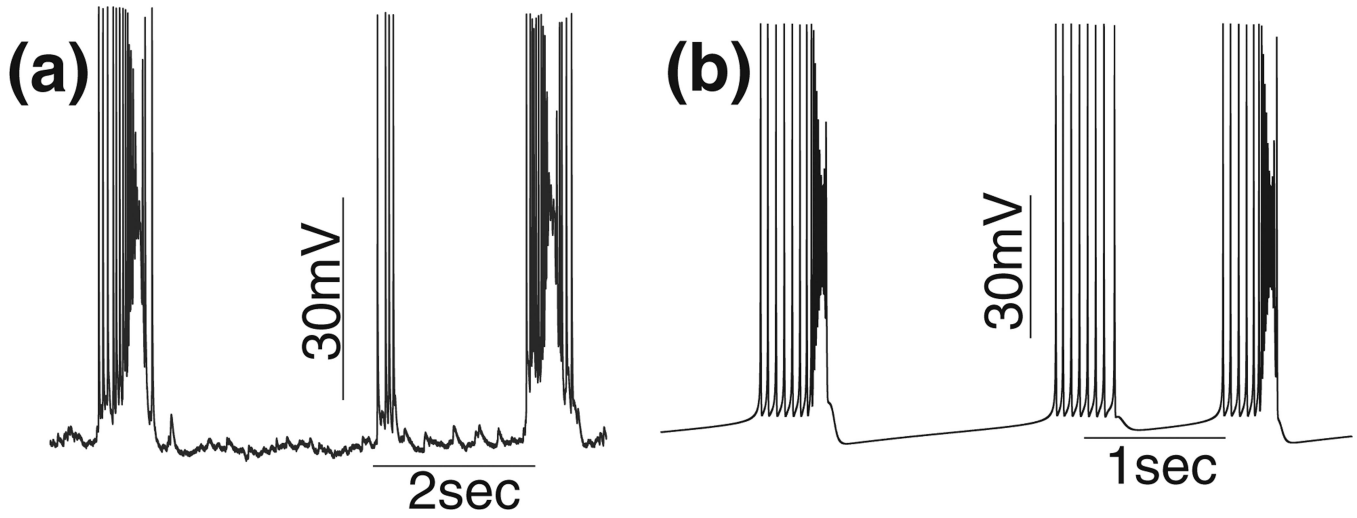

Fig. 14.

Silent phases following DB bursts have longer durations than those following square-wave bursts. Panel (**a**) shows a sample recording from a preBötC cell that consistently exhibited both square-wave and DB bursts. Panel (**b**) shows a typical trace from region *. Even though the time scale is not the same, the relative differences between the silent phases in the model agree well with the data

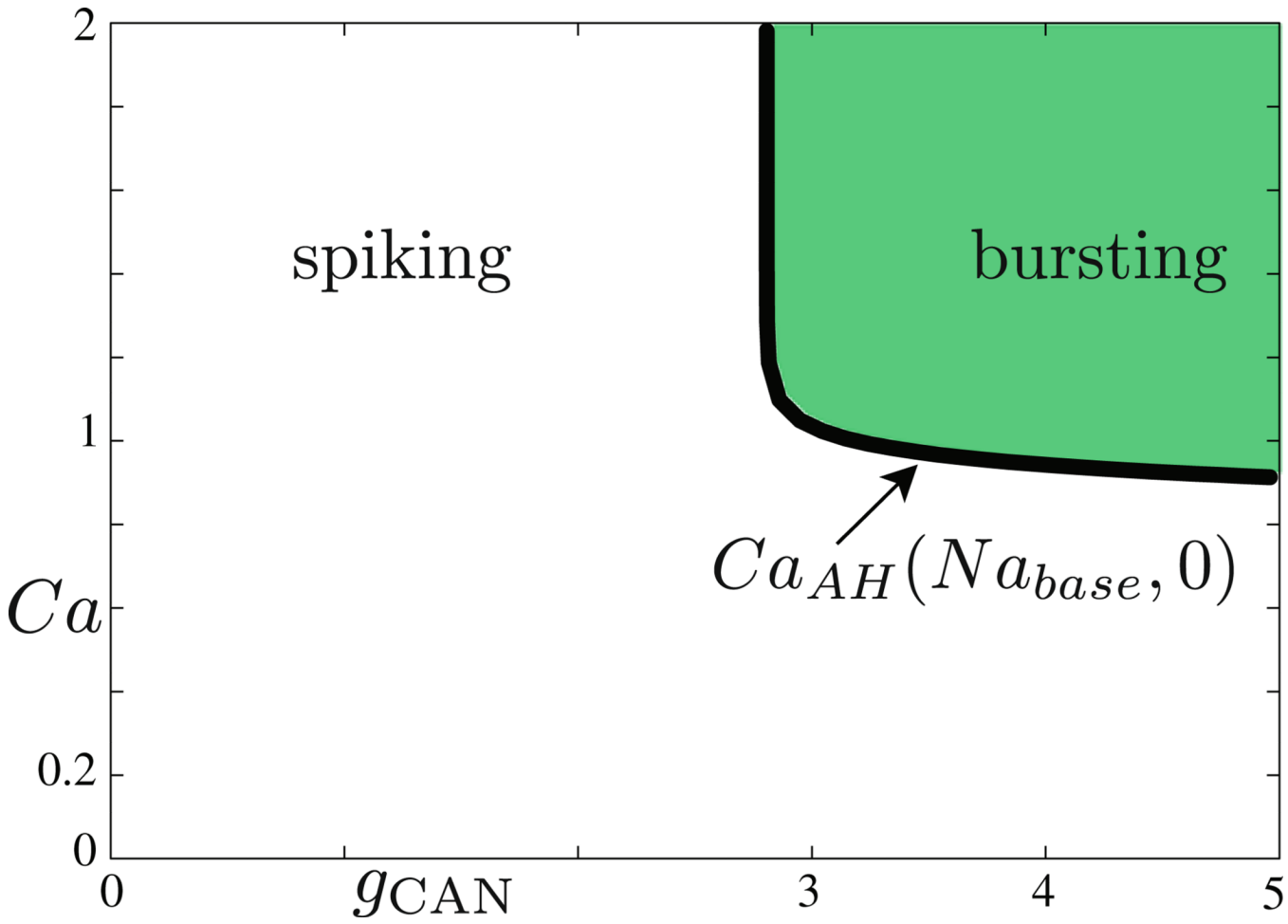

Fig. 15.

$Ca_{AH}(Na_{\mathrm{base}}, 0)$ as a function of g_{CAN}, with $g_{\mathrm{NaP}} = 3$. For fixed g_{CAN}, if $Ca_{AH}(Na_{\mathrm{base}}, 0)$ is below the maximal value of Ca attainable by the full system, the full system can exhibit a DB burst. Lowering g_{CAN} causes $Ca_{AH}(Na_{\mathrm{base}}, 0)$ to blow up, so that depolarization block is never realized, resulting in tonic activity

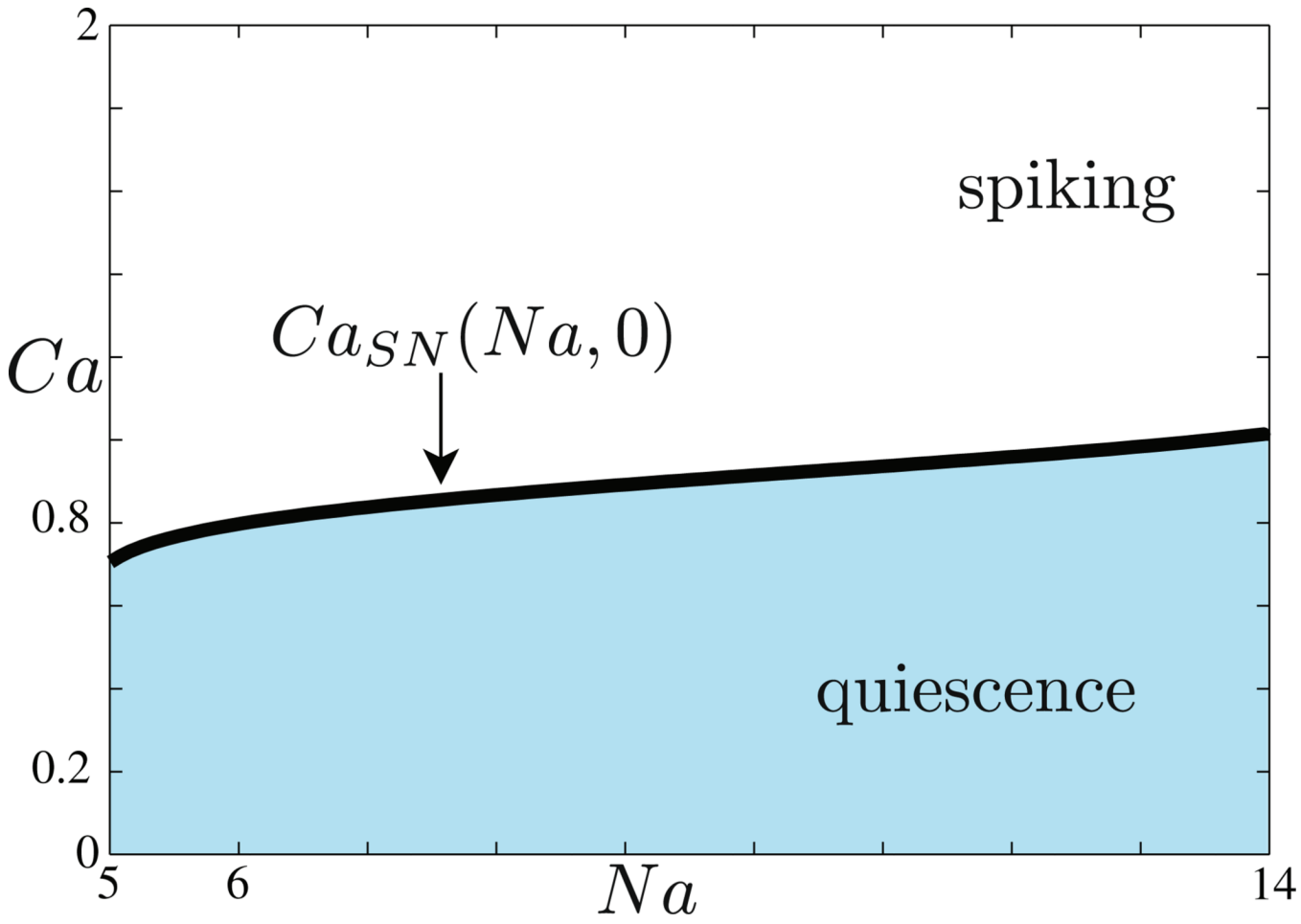

Fig. 16.

$Ca_{SN}(Na, 0)$ plotted for $g_{CAN} = 2.5$ and $g_{NaP} = 3$, a value for which the full system's *Ca* coordinate cannot attain $Ca_{AH}(Na_{base}, 0)$. For (*Na, Ca*) below $Ca_{SN}(Na, 0)$, the full system exhibits quiescence, while above it, the full system exhibits tonic spiking

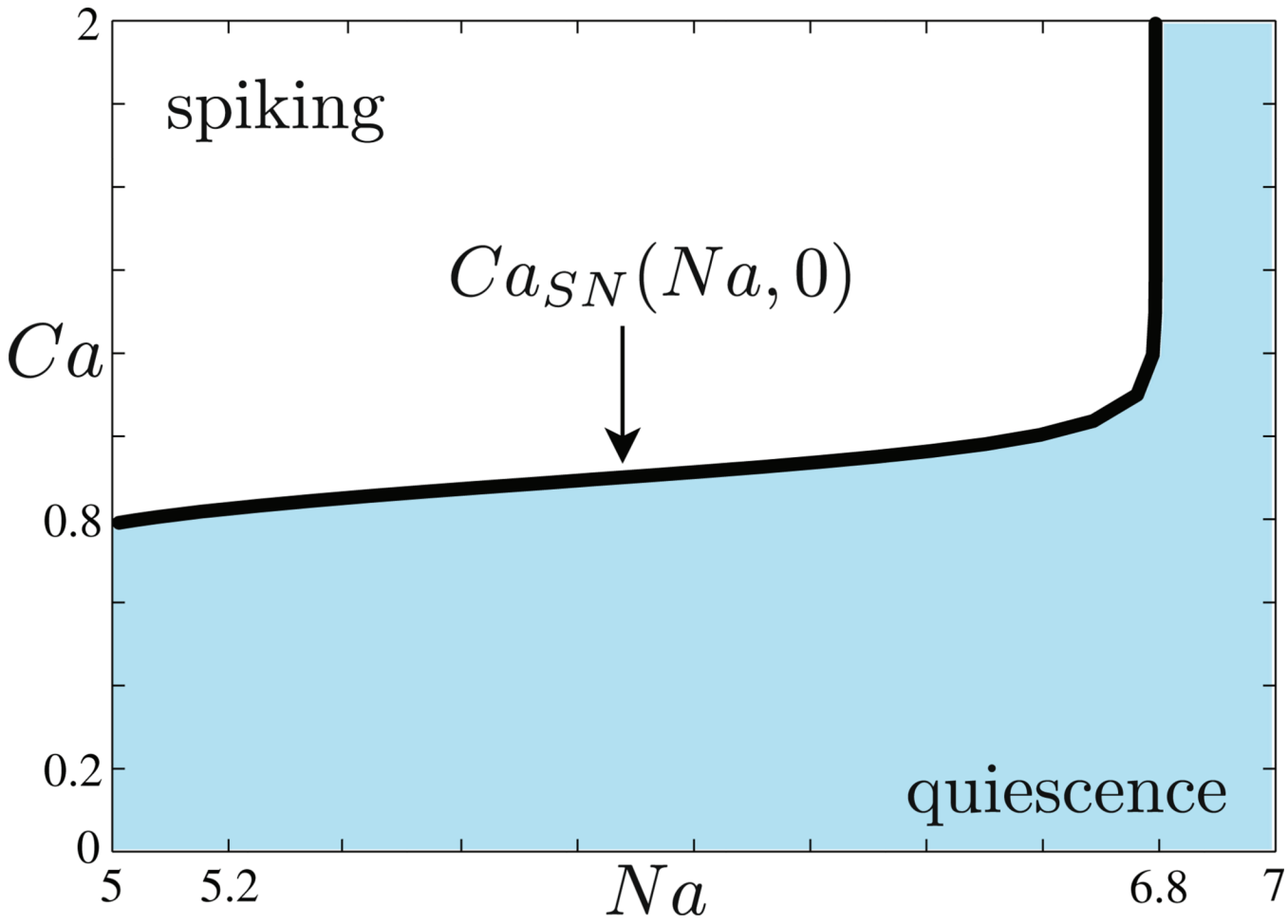

Fig. 17.

$Ca_{SN}(Na, 0)$ plotted for g_{NaP} and g_{CAN} corresponding to region V. Note that for values attainable by Na during tonic spiking, $Ca_{SN}(Na, 0)$ blows up. Using the approximation $Ca_{HC}(Na, 0) \approx Ca_{SN}(Na, 0)$, we conclude that $Ca_{HC}(Na, 0)$ blows up for finite Na as well. For (Na, Ca) below $Ca_{SN}(Na, 0)$ the full system's dynamics corresponds to quiescence, while for those above $Ca_{SN}(Na, 0)$ the full system exhibits tonic spiking

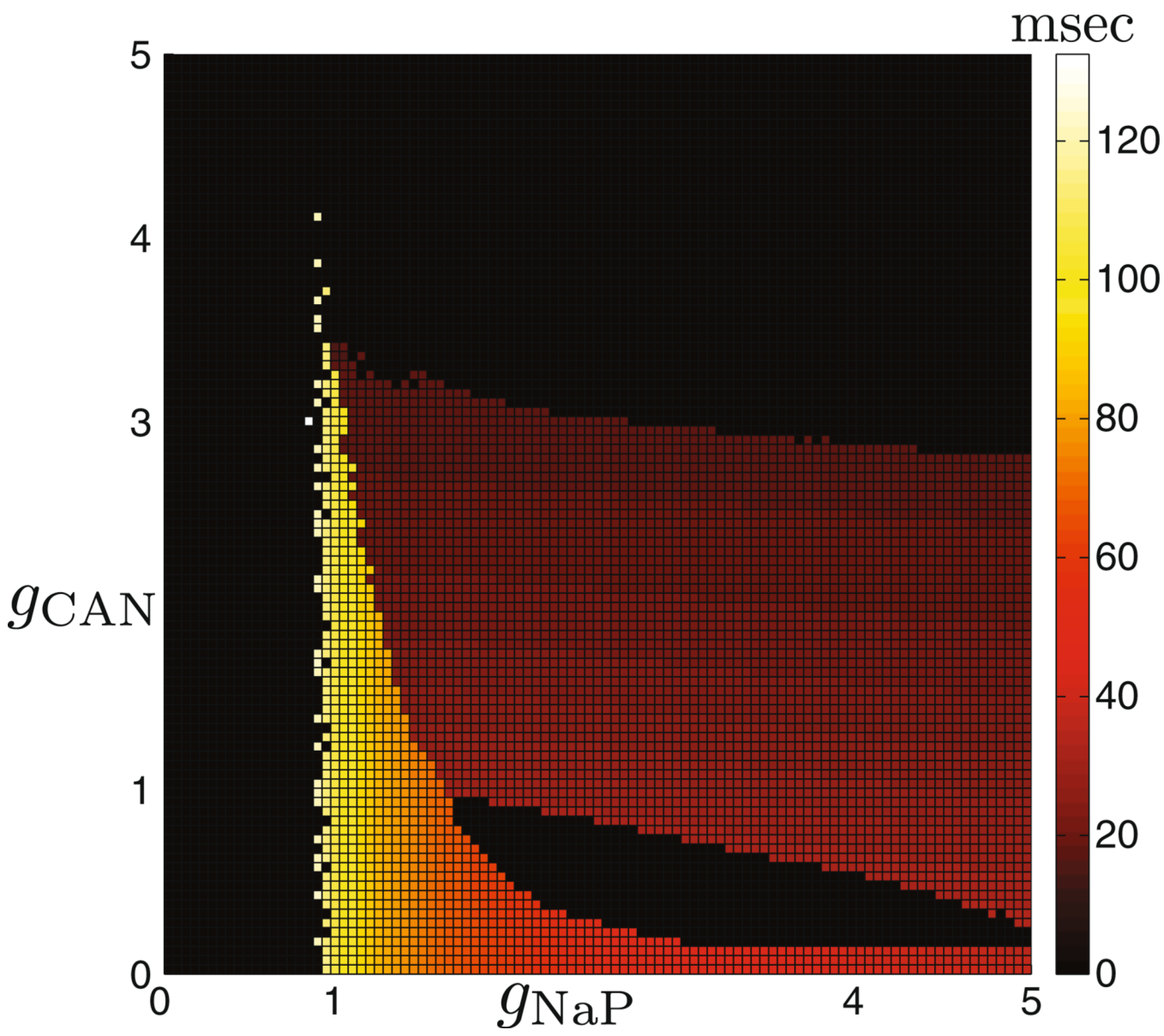

Fig. 18.

Mean interspike interval (ISI) for tonically active model neurons. *Black regions* indicate that the model neuron was not tonically active. Note the sharp change between high ISI and low ISI within the tonic spiking dynamics that occurs at some $g_{CAN} \in (1, 3.5)$ for each $g_{NaP} \in (1, 2)$

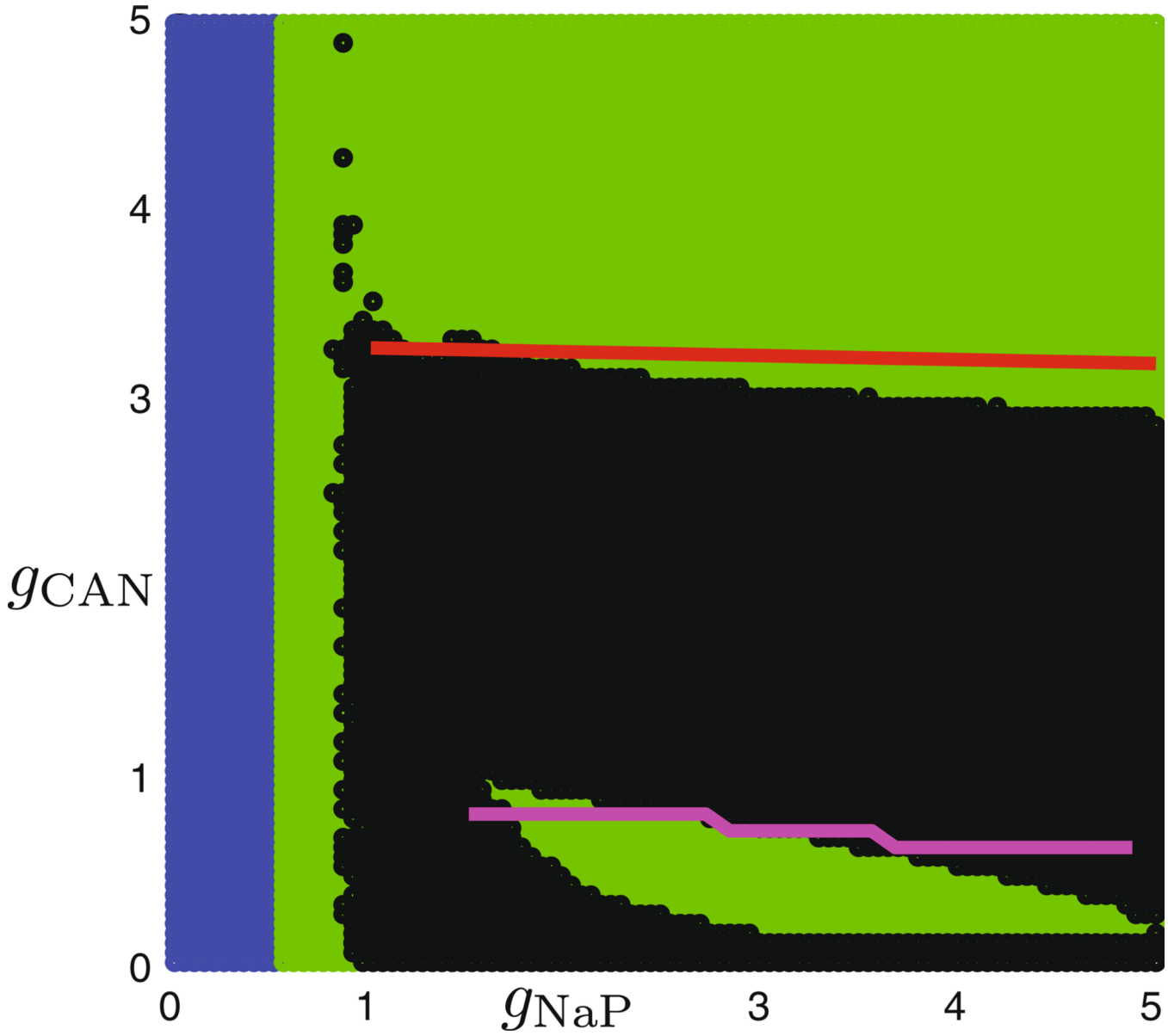

Fig. 19.
Numerical approximations to the boundaries between regions III and IV (red), and IV and V (magenta), as described in Sections 6.4 and 6.5, respectively

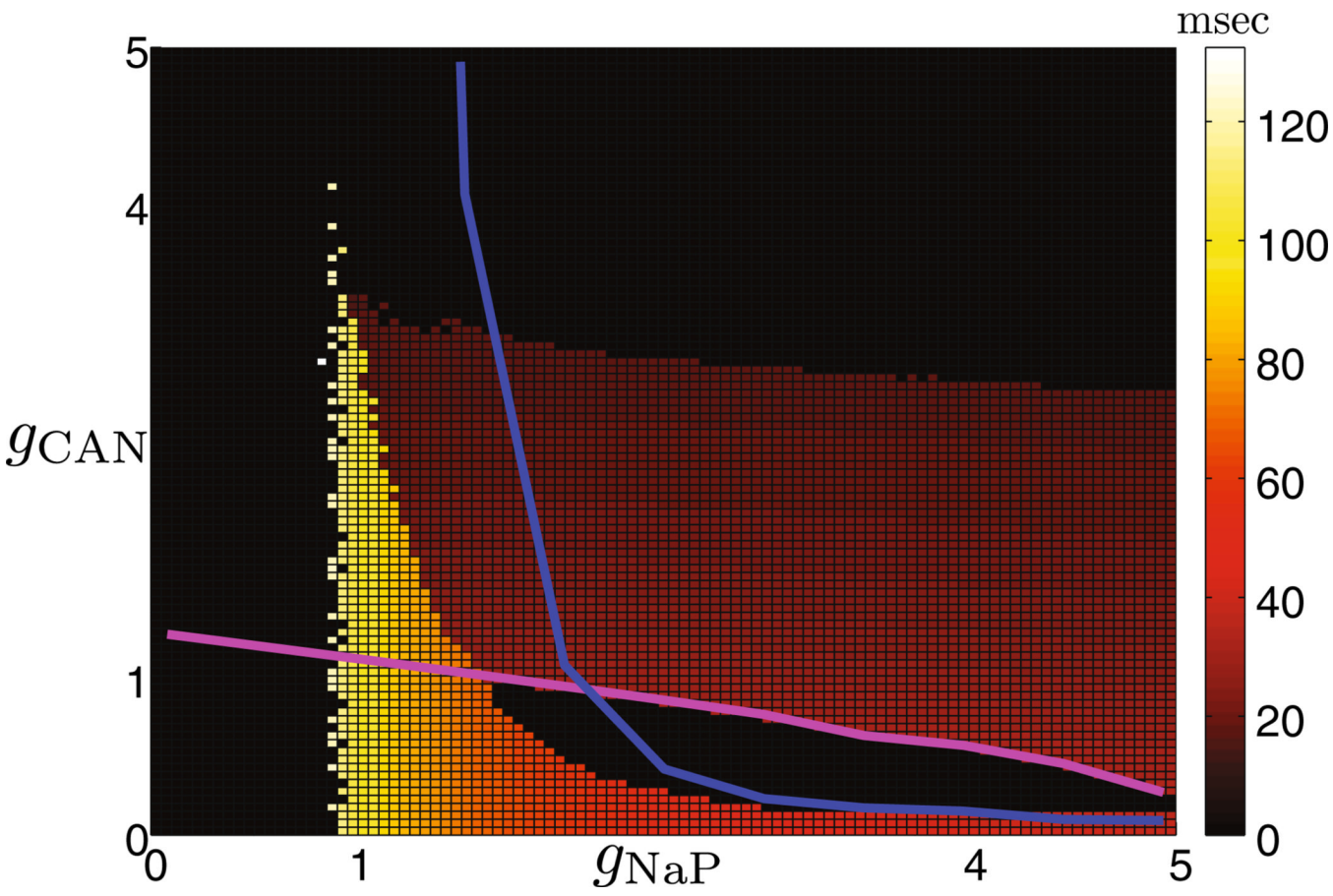

Fig. 20.

Locations of torus bifurcations of tonic solutions from region IV found by decreasing g_{CAN} as described in Section 6.5. For (g_{NaP}, g_{CAN}) above the *magenta curve*, there are stable tonically active solutions. Also, for (g_{NaP}, g_{CAN}) below the *blue curve*, there is a second family of stable solutions with tonic activity

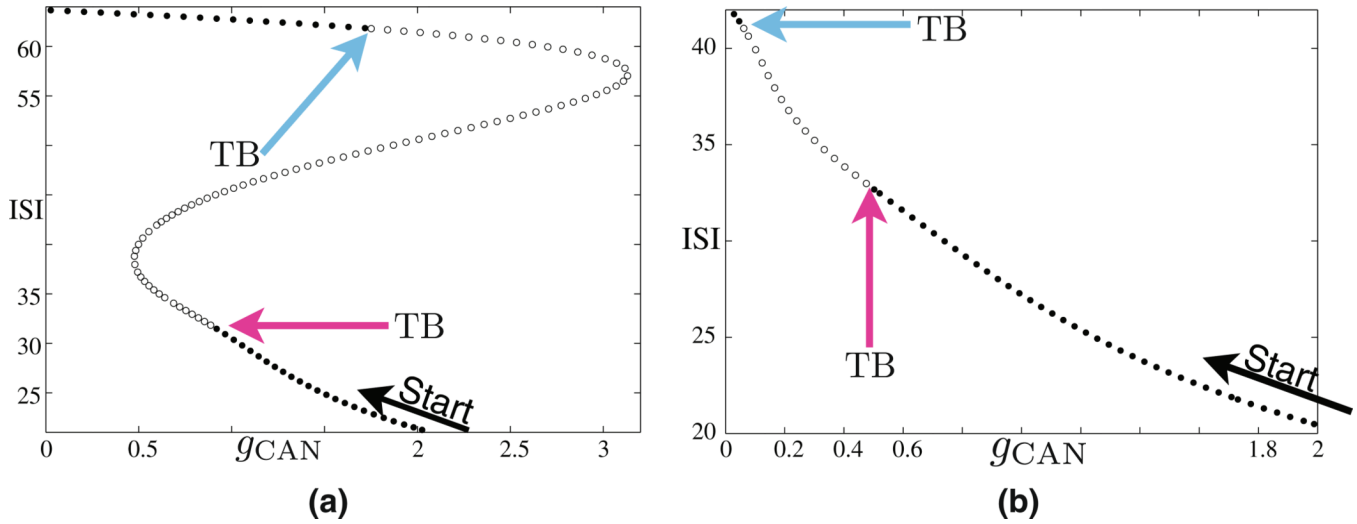

Fig. 21.

Two examples of the bifurcation analysis described in Section 6.5. *Solid dots* correspond to stable tonically active solutions with the corresponding ISI, and *open circles* are unstable tonic solutions. In each panel above, the continuation analysis begins at $g_{CAN} = 2$ and initially g_{CAN} decreases. The first torus bifurcation found is labeled as TB with a *magenta arrow* and the second one is labeled with a *blue arrow*. For Panel (**a**), g_{NaP} was fixed at $g_{NaP} = 1.8$. Note that after locating the first torus bifurcation the analysis encountered a LPPO bifurcation and the algorithm increased g_{CAN} until another LPPO was encountered. Decreasing g_{CAN} again eventually yielded another torus bifurcation at a higher g_{CAN} value than the first. For Panel (**b**), g_{NaP} was fixed at $g_{NaP} = 4$. We note that in Panel (**b**), the continuation analysis was monotonic in g_{CAN}

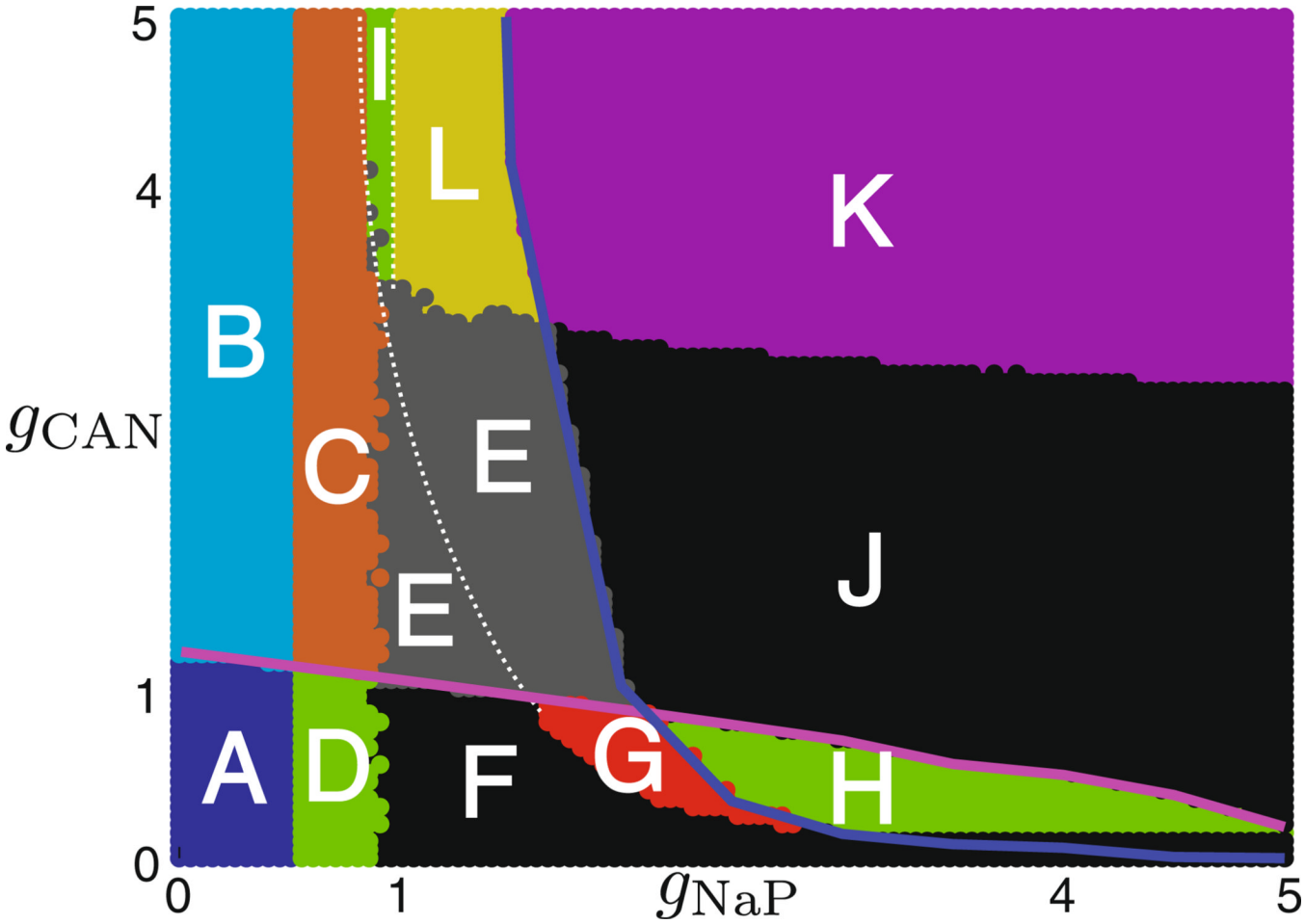

Fig. 22.

Partitioning of parameter space based on bistability analysis. The colors only establish the boundaries of regions A–L

Table 1

Common parameter values for Eqs. (1)–(8)

Parameter	Value	Parameter	Value	Parameter	Value	Parameter	Value
α	6.6×10^{-5} mMpA^{-1}ms^{-1}	g_K	30 nS	Na_{base}	5 mM	$\bar{\tau}_{hp}$	1 ms
Ca_{base}	0.05 μM	g_L	3 nS	r_{pump}	200 pA	$\bar{\tau}_m$	1 ms
C_m	45 pF	g_{Na}	160 nS	σ_{CAN}	−0.05 μM	$\bar{\tau}_n$	30 ms
E_{K}	−75 mV	g_{syn}	2.5 nS	σ_h	5 mV	τ_s	15 ms
E_{Na}	65 mV	I_{app}	0 mV	σ_{hp}	6 mV	θ_h	−30 mV
ε_{Ca}	0.0007	k_{IP_3}	1200 μMms^{-1}	σ_m	−8.5 mV	θ_{hp}	−48 mV
ε_{hp}	0.001	k_s	1	$\sigma_{m,p}$	−6 mV	θ_m	−36 mV
E_{CAN}	0 mV	k_{Na}	10 mM	σ_n	−5 mV	θ_{m_p}	−40 mV
E_{syn}	0 mV	k_{Ca}	22.5 ms^{-1}	σ_s	−3 mV	θ_n	−30 mV
E_L	−61 mV	k_{CAN}	0.9 μM	$\bar{\tau}_h$	15 ms	θ_s	15 mV

Table 2

Dynamics observable in regions of Fig. 22

Region of Fig. 22	Solutions corresponding to regions of Fig. 6
A	I
B	I, IV
C	II, IV
D	II
E	IV, VI
F	IV
G	V, VI
H	V
I	*, IV, VI
J	IV
K	III, IV
L	III, IV, VI